Università degli Studi di Padova

Dipartimento di Fisica e Astronomia "Galileo Galilei"

Master Thesis in Astrophysics and Cosmology

Binaries in Star Clusters: NGC 2158

Supervisor
Prof. Antonino P. Milone
Università di Padova

Master Candidate
Anastasia V. Marchuk
Student ID: 2106915

Academic Year 2024/2025

If, on the other hand, we have recourse to the simplicity of the known effects of attraction, and admit the two stars of our present double star to be united in one system, all the foregoing difficulties of accounting for the observed phenomena will vanish.

Herschel, 1803

Abstract

A large fraction of stars in both the solar neighborhood and star clusters are a part of binary systems, so developing a complete understanding of binaries is essential in order to properly describe stellar structure, stellar evolution, and the dynamical history of clusters. Despite extensive study of binaries in star clusters, key open questions still exist. In particular, photometric binaries among low mass stars are largely unexplored. While the binary fraction in field stars has a strong correlation with stellar mass, studies focused on star clusters suggest a nearly constant fraction across the limited mass range investigated to date. Additionally, the mass function of very low mass stars remains largely unconstrained among clusters older than a few hundred Myr.

In this work, I analyze deep, multi-epoch images of the intermediate age open cluster NGC 2158, obtained with the Wide Field Channel of the *Hubble Space Telescope* Advanced Camera for Surveys. I derived high precision photometry and proper motions using software developed by Jay Anderson. This data enabled, for the first time, a detailed study of binary stars in this cluster as well as the determination of the luminosity and mass functions to $\sim 0.1 M_\odot$.

The best fit isochrone for this cluster gives an age of 1.9 Gyr and [Fe/H] = -0.03. The color magnitude diagram reveals a well defined binary sequence that is clearly distinguishable down to the lowest stellar masses. From this dataset, I measured the binary fraction over the deepest mass range investigated so far, finding a value of 19%, comparable to that observed in other open clusters. I also find a strong mass dependence: the binary fraction decreases from ∼26% at 1.08 $M_\odot$ to ∼12% at 0.22 $M_\odot$. This trend is consistent with that observed in the solar neighborhood and the Galactic field, suggesting that binaries in clusters and in the field share similar properties, in contrast with some earlier results.

The mass function of NGC 2158 is best described by three regimes: high-mass stars ($\alpha = -2.27$), low-mass stars ($\alpha = -1.24$), and very low-mass stars ($\alpha = 0.03$). The change in slope at $\log(M/M_\odot) \approx -0.05$ separating the high and low mass regimes is in agreement with Cordoni et al. [2023], but there is a deficit of stars in the very low mass range. This study presents the first combined analysis of the binary fraction and mass function across such an extended mass range in this cluster, providing new insights into the binary population and very low-mass stars in open clusters.

Contents

Listing of figures

Listing of tables

1
Introduction

1.1 Stellar Clusters

Star clusters are large groups of stars that are gravitationally bound together. Traditionally, stellar clusters were considered examples of simple stellar populations, meaning that the cluster stars formed at the same time with the same chemical composition [Renzini and Buzzoni, 1986]. For a time, it was thought that clusters might consist entirely of single stars, and that any binaries in a cluster formed dynamically through capture. As it became clear this was not the case, the study of binaries and calculation of their fraction of the population has become increasingly important [Hut et al., 1992].

Because stellar clusters are distinct, dynamically bound groups of stars, they are a perfect environment to use when studying stellar evolutionary sequences. Cluster color magnitude diagrams show distinct features that can be used to find the age of the cluster, such as the white dwarf cooling sequence or main sequence turn off point. Other features, like the red giant branch bump, can be indicators of the amount of reddening affecting the photometry of a cluster. Spectroscopic analysis can be used to find the metallicity of stars in a cluster. However, metallicity also has a strong effect on the color magnitude diagram, shifting stars to the right and lowering the inclination of the red giant branch as metallicity increases. A cluster with a more metal rich population of stars will be redder and fainter than a metal poor cluster. The oldest clusters are used in Galactic archaeology to study the early universe, particularly those in the halo of the Milky Way. They are part of the search for extremely metal poor stars, which are considered the most likely candidates for the first stars that formed in the universe [Frebel and Norris, 2015].

Star clusters are sorted into two types: globular clusters and open clusters. Globular clusters are often very old, and are among the oldest objects in the universe for which we can get a reliable age determination. They typically contain millions of stars. Open clusters are typically much younger, and contain up to several thousand stars. Since they are more loosely gravitationally bound, they eventually dissociate on a faster timescale than globular clusters [Seeds and Backman, 2016]. This work focuses on NGC 2158, an open cluster that is approximately 1.9 billion years old.

1.2 Binary Systems

Binary stars are a crucial element of any stellar population. A large fraction of stars are in binary systems: in particular, Cordoni et al. [2023] found that among 78 Galactic open clusters, the binary fraction was between $\sim 15\%$ and over 60%. In the solar neighborhood alone, more than half of all stars are in binary systems [Duquennoy and Mayor, 1991]. Binaries, therefore, must have an important effect on the dynamical history and evolution of clusters, as well as star formation and stellar evolution in a population of stars. With such a high percentage of a cluster's stars in binaries, this phenomenon must be accounted for in terms of affecting the total number of stars in order to properly determine the mass and luminosity functions [Cordoni et al., 2023].

The evolution of binary systems can eventually lead to the creation of exotic objects, that can even remain in binary systems. The outcome changes depending on the physical properties of each system: for example, cataclysmic variables are close binary systems that consist of a white dwarf that is accreting matter from a cool, low mass secondary star. The accretion disk creates UV and X-ray emission, and bright outbursts called novae can occur when accretion on the white dwarf creates a thermonuclear reaction. Blue straggler stars form from the merging of the two stars in a binary system. These can form through mass transfer over time, when one star becomes a red giant and fills its Roche lobe, and the other star begins stripping material from the red giant's envelope. They can also form through the collision of the two stars. Blue stragglers appear brighter and bluer than stars at the main sequence turn off. The different formation routes mean that the chemical compositions of the resulting stars can differ, which may lead to the creation of two distinct sequences on the CMD. Other objects, such as X-ray binaries, are "normal" stars with neutron star companions [Milone et al., 2012].

Binaries are very relevant to the study of cluster dynamics, as well. The development of N-body problems that model cluster dynamical evolution began with the single stars assumption, in part because this is quite an efficient modeling method (e.g., Larson [1970]), and part because this was the understanding of cluster composition at the time. However, binaries and their comparatively larger cross sections of interaction with other stars in the cluster [Mohandasan et al., 2024] take a large role in the ejection of stars from clusters, and generally in the disruption of the system and distribution of kinetic energy among cluster members [Heggie, 1975]. The denser cluster centers that form over time as lower mass stars are scattered outwards and higher mass stars fall inwards tend to produce exotic objects, as mentioned previously (Mohandasan et al. [2024] and references therein).

Many methods have been developed over the years to detect binary stars and distinguish them from normal stars. The first binary stars were detected after careful observation of double stars revealed after 25 years that some of them were orbiting each other [Herschel, 1803]. Double stars are those that appear very close to each other visually in the sky. We now call these visual binaries, since they can be resolved either by eye or with other methods. Due to the astronomical distance scale of stellar clusters, this method is not suitable for the purposes of binary identification. Other methods include spectroscopic identification, which studies the spectra of stars to look for radial velocity variation indicating the orbit of a second star, and photometric variability, which looks for changes in emitted light from a star caused by a fainter star - brighter star pair. Although these methods can be used to identify individual binary systems and their characteristics, their biases and limitations prevent them from being useful for this work. Both are limited to short period binaries, for example. For these reasons, this work uses a photometric method.

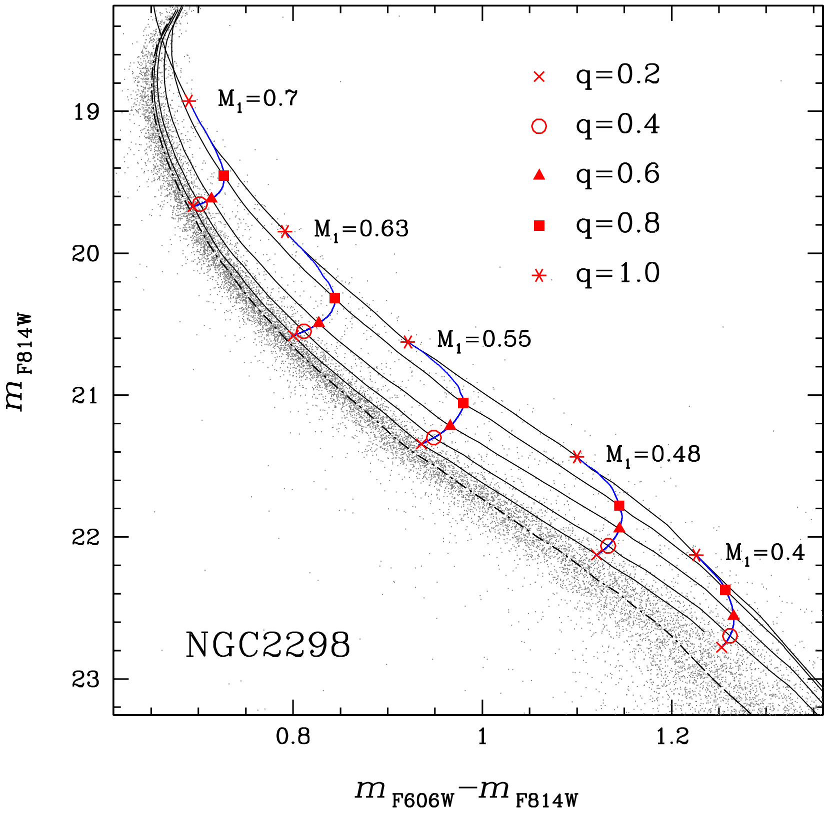

Figure 1.1: Model MS-MS binary sequences with different mass ratios for NGC 2298. The dashed-dotted line is the main sequence ridge line while, continuous black lines indicate the sequences of constant q and blue lines mark sequences of constant m_1. Figure and caption adapted from Milone et al. [2012].

Stellar clusters are crowded environments, and binaries in clusters are necessarily too close to each other to be resolved individually. The light from the two stars blend together into a single source that is comparatively redder than single stars from the main sequence [Cordoni et al., 2023]. The magnitude (m_{bin}) of this source can be calculated as:

$$m_{bin} = m_1 - 2.5 \log \left(1 + \frac{F_1}{F_2} \right), \tag{1.1}$$

where m_1 and m_2 are individual stellar magnitudes, and F_1 and F_2 are the stellar fluxes [Milone et al., 2012].

The resulting m_{bin} is brighter than the main sequence, with its luminosity dependent on the mass ratio $q = M_1/M_2$, where M_1 and M_2 are the masses of the two binary stars. This creates a binary sequence to the red side of the main sequence fiducial line, that can be analyzed to find the fraction of binaries in a stellar population. As an example, Figure 1.1 from Milone et al. [2012] demonstrates the relation between m_1 and q on a CMD of NGC 2298, showing how the position of m_{bin} changes as q changes for different values of M_1. While binaries with a large mass ratio move relatively far from the main sequence, binaries with a mass ratio smaller than $q = 0.5$ are difficult to detect. They do not move very far from the main sequence, and therefore are indistinguishable from the main sequence itself using this analytical method.

Photometry is a very powerful tool for identifying binaries in open and globular clusters, and for constraining their mass, mass-ratio, and radial distributions. It has been used to analyze the binary fraction in Hubble Space Telescope (HST) imaging for roughly one hundred Galactic and Magellanic Cloud clusters (e.g., Sollima et al. [2007], Milone et al. [2012], Mohandasan et al. [2024]), though typically only within cluster cores and for stars more massive than ~0.5 solar masses ($M_\odot$). Gaia releases have expanded binary studies in open clusters for the brightest, most massive members. This method requires observations in only two filters, used to create the CMD. Additionally, there is no reliance on any system properties in the way period or inclination would affect the spectroscopic or variability methods. The only limitation on system properties is the mass ratio, whereby stars with a very low mass ratio are not distinguishable from single stars under this method. Perhaps most importantly, thousands of stars can be investigated simultaneously using the CMD [Cordoni et al., 2023].

2
Data Reduction

This section describes the method I used to refine the raw data from HST into a photometric catalog that can be used to create a CMD. It also discusses the instrumentation from HST, and the dataset and filters used.

All codes used in the reduction of data that are cited by name (e.g. `img2psf`) are one of the FORTRAN programs developed by Anderson et al. [2008] and their newer version KS2 (see Milone et al. [2023]), or an adapted version of one of these. This also applies to Section 3.

2.1 Instrumentation

This work uses photometric data from HST, which is a joint program between NASA and ESA. The HST is a space-based telescope that observes from ultraviolet to infrared wavelengths. The primary mirror is 2.4m in diameter. It was launched into low-Earth orbit in 1990, and serviced several times by astronauts to repair or replace instruments. Since HST is located above Earth's atmosphere, it does not experience problems with seeing due to atmospheric interference or weather conditions. It is able to observe in the ultraviolet part of the spectrum since there is no atmosphere to block these wavelengths. There is also less interference from the Earth's variable temperature conditions, and other noise sources, in the infrared [HST - About]. This allows high-resolution imaging, which is

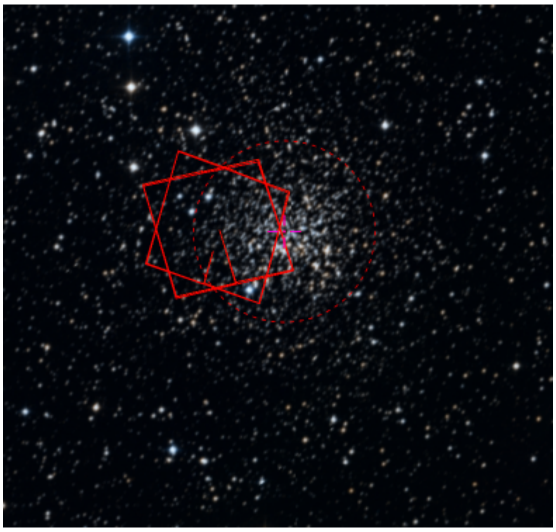

Figure 2.1: HST observation field of view plotted over an image of NGC 2158 (MAST Portal).

required when studying crowded fields like stellar clusters.

Currently aboard the HST are three cameras, two spectrographs, and guidance sensors. For this work, I used data taken by the Advanced Camera for Surveys (ACS), installed in 2002. The ACS has three different channels: wide field, high resolution, and and ultraviolet. This work used the Wide Field Channel (together, ACS/WFC). The WFC is capable of imaging in the visible to near-infrared [Stark, D. V., et al.]. This dataset used the filters F606W and F814W, in the wavelength ranges of 462nm to 718nm and 687nm to 963nm respectively.

2.2 Dataset

The data was taken in 2005 and 2006 in the F606W and F814W filters, as described in Tables 2.1 and 2.2. This dataset is from observations for HST Proposal 10500, with principal investigator L. Bedin. The fields of view of the two epochs of observation can be seen overlaid on an image of NGC 2158 in Figure 2.1, from AstroView in the MAST Portal[1].

Included in the dataset are two types of fits files that I used: *flc.fits and *drc.fits. Each has had different processing applied to it during the ACS calibration pipeline. The files with names ending in drc are drizzled images that

[1] https://mast.stsci.edu/portal/Mashup/Clients/Mast/Portal.html

F606W: 2005			F606W: 2006		
Filename	**Date Obs.**	**Exp. Time**	**Filename**	**Date Obs.**	**Exp. Time**
j9cx01cfq	24/10/05	1145	j9cx02otq	09/11/06	0
j9cx01clq	24/10/05	1150	j9cx02ouq	09/11/06	1145
j9cx01crq	24/10/05	1150	j9cx02ozq	09/11/06	20
j9cx01cwq	24/10/05	20	j9cx02p0q	09/11/06	1150
j9cx01cxq	24/10/05	1150	j9cx02p5q	09/11/06	20
j9cx01d2q	25/10/05	20	j9cx02p6q	09/11/06	1150
j9cx01d3q	25/10/05	1150	j9cx02pcq	09/11/06	1150
			j9cx02piq	09/11/06	1150

Table 2.1: File name, date of exposure, and exposure time in seconds for observations in the filter F606W. Left three columns display the 2005 epoch, right three columns display 2006 epoch.

F814W: 2005			F814W: 2006		
Filename	**Date Obs.**	**Exp. Time**	**Filename**	**Date Obs.**	**Exp. Time**
j9cx01ceq	24/10/05	0	j9cx02owq	09/11/06	1130
j9cx01chq	24/10/05	1130	j9cx02p2q	09/11/06	1150
j9cx01ckq	24/10/05	20	j9cx02p8q	09/11/06	1150
j9cx01cnq	24/10/05	1150	j9cx02pbq	09/11/06	20
j9cx01cqq	24/10/05	20	j9cx02peq	09/11/06	1150
j9cx01ctq	24/10/05	1150	j9cx02phq	09/11/06	20
j9cx01czq	24/10/05	1150	j9cx02pkq	10/11/06	1150
j9cx01d5q	24/10/05	1150			

Table 2.2: As Table 2.1, but for the F814W filter.

have been calibrated, geometrically corrected, and CTE corrected. Drizzling is a method of linear combination of images. Files with names ending in flc have been fully calibrated through the ACS calibration pipeline including CTE correction, but are otherwise the original images and may still contain errors like oversaturated pixels due to cosmic rays. CTE is charge transfer efficiency, a measure of how efficiently a CCD transfers charge between pixels during the readout process. Due to the aging of the instruments, and the harsh space environment, the CTE will become worse over time.

2.3 Finding the Point Spread Function

To create a catalog of stars, we need to know the position and magnitude of each star in the observations. To find this, I first created an effective point spread function (PSF) that made a model of all the stars in an image. A PSF represents how the light from an object is imaged by a detector. Because every detector is slightly different, and even different parts of a detector will image more effectively than other parts, the PSF is specific to the instrument and the filter used. To make a PSF for the CCD, we need to know the position and flux of each star, but to find the position and flux of each star we need a PSF. This creates a degeneracy. To work around this, we start the process for each image using a generic PSF that is based on the known properties of the detector (the ACS/WFC) and the filter (F606W or F814W). An individual PSF is created from each image. The first step uses a version of the FORTRAN program `img2psf` adapted for the ACS/WFC instrument. The first run of this code should only include bright and well-isolated stars, so that the PSF model can find as accurate a star shape as possible. It allows adjustment of the following parameters:

- **`HMIN`**`: dominance of peak` (minimum number of pixels between sources)
- **`FMIN`**`: min peak excess` (minimum value that counts as stellar flux)
- **`PMAX`**`: max pix included` (maximum value that counts as stellar flux)
- **`QMAX`**`: max badness included` (q is the quality fit, QMAX is maximum q value)
- **`NSIDE`**`:` (number of regions an image should be divided into e.g. 1x1, 2x2, up to 5x5)
- **`PSFFILE`**`:` (first run uses archive file for the corresponding filter for the image)

The final input for the program is the image upon which the PSF is being calculated. I used `HMIN = 13`, `FMIN = 5000`, `PMAX = 54000`, `QMAX =0.3`, and `NSIDE = 2`. The `PMAX` value is just below the pixel saturation value of 60,000. The program iterates through a fitting procedure to create the final PSF. The first

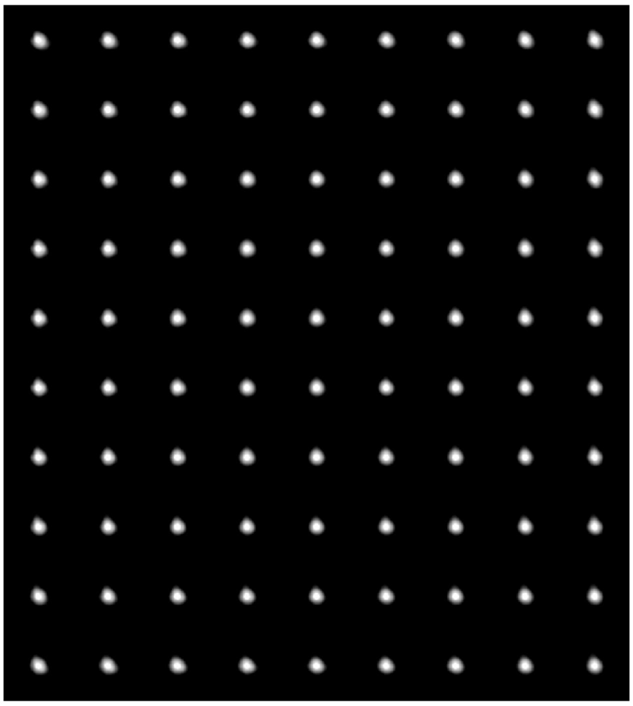

Figure 2.2: The PSF model created for an image in F606W in 2005 using `img2psf`.

iteration uses the archive PSF based on general properties, and each additional iteration uses the model from the previous iteration in order to improve the result. The program creates a grid of PSF models across the entire image so that it can correct for error factors from different areas of the CCD itself depending on the location of the star being measured (Figure 2.2).

This code outputs the generated PSF model, and a `.xym` file, listing information on all the bright stars in the image such as position and magnitude.

The next step is running `img2xym`, customized for ACS/WFC. The inputs are nearly the same as the previous one, excluding `QMAX` and `NSIDE`. I used `HMIN = 3`, `FMIN = 100`, and `PMAX = 10e9`. At this point, since we are not excluding oversaturated pixels, `PMAX` is set much larger than the saturation value to ensure everything is collected. `FMIN` is set much lower than the value in the previous step (100, as opposed to 5000) in order to collect faint signals, but not so low as to misidentify noise pixels as sources. `HMIN` is also lower, because the goal is no longer to collect only well-isolated stars, but all sources in the image.

The input PSF file for each image should be the corresponding one generated by `img2psf` in the previous step. This will also output a `.xym` file, but a much larger one as it includes both bright well isolated stars, and fainter or less well measured sources.

2.4 Quality Fit

The `.xym` files are catalogs of all stars and star-like objects in which x and y are position in the reference frame of the image, m is the magnitude in instrumental units (photon count), and q is the quality fit. Quality fit describes how well the PSF fits a star, with 0 corresponding to a star perfectly measured by the PSF. The closer to 1, the worse the fit. The value q is defined as

$$qfit = \frac{\sum_{i,j} \text{pix}_{i,j}\text{PSF}_{i,j}}{\sqrt{\sum_{i,j} \text{pix}_{i,j}^2\text{PSF}_{i,j}^2}} \tag{2.1}$$

in Milone et al. [2023]. When creating a stellar catalog it is important to exclude light sources that are not stars, because we are only interested in potential cluster members. Additionally, when matching all the images into a common reference frame, the transformation needs to be as accurate as possible. Any outliers or unrelated objects need to be removed as they could create an incorrect match. I do this by creating a plot of quality fit over magnitude, as shown in Figure 2.3.

Outliers were selected and removed semi-manually. As Figure 2.3 shows, the bright stars all have q relatively close to zero. The q value increases for well-measured stars as magnitude decreases. Eventually, lower than a certain magnitude value, the PSF model poorly fits faint stars and their q values become large. Anything fainter than -6.5 magnitudes was accepted automatically, as their measurements will be refined later on in the process. Anything above -13.5 magnitudes is also automatically accepted.

Separate from the coherent spread of well-fit stars is a crowded, typically somewhat oval-shaped region of outliers that could be galaxies, cosmic rays, artifacts, etc. To remove those, I split the remaining sources into bins of 0.5 magnitude from -13.5 to -6.5 (for F814W), found the median value for each bin, and rejected anything greater than 2σ from the median. For F606W, the process is the same, except everything fainter than -7 magnitudes is accepted automatically,

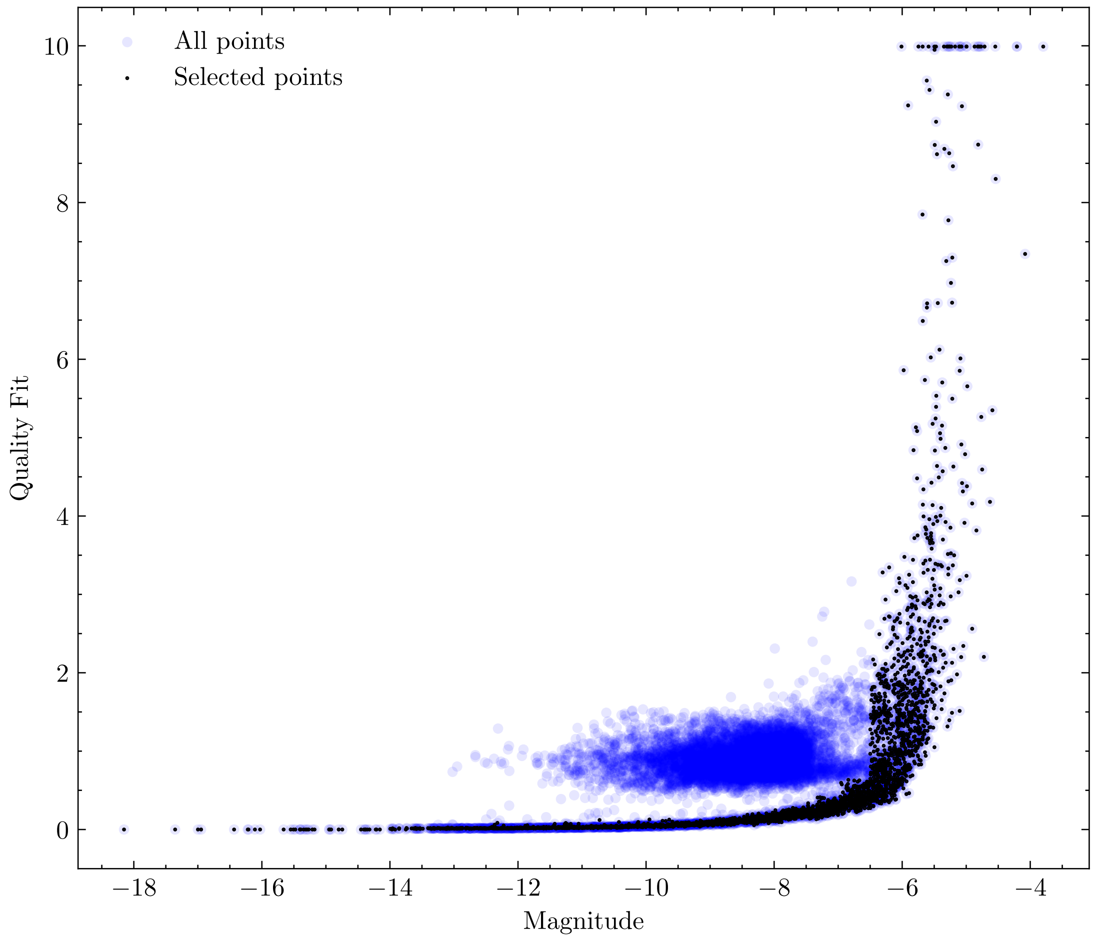

Figure 2.3: Quality fit over magnitude. The blue points are all the points in the `.xym` file, and the black points are those selected for the next step of data analysis. This file is `j9cx01ckq` in the F814W filter.

and specifically the range from -8 to -7 is split into bins of 0.25 instead of 0.5 magnitudes. This choice was made because the slope of increasing q with decreasing magnitude was different than F814W, and it required smaller bins to properly select stars to keep. It is important to remove as many outliers and bad sources as possible. However, if there are some remaining outliers that do not show up in every single image, they will be lost during the coordinate transformation process as they will have no matches. This process is done for every image in each filter, and as an output produces the `.xyms` file.

3

Photometry

The stars in each file have been selected and measured, but their coordinates are in the reference frame of the image itself. Those coordinates may be offset from each other, even between two images from the same filter and epoch. For this reason, the files must be carefully merged before creating a final catalog. Then, the coordinates need to be transformed into the *GAIA* reference frame, and the magnitudes have to be properly calibrated into the Vega mag system by accounting for variations in measurement from exposure time dependencies, data loss due to aperture and pixel size, and the zeropoint corrections for the specific dates of observation.

Once the photometry is calibrated, it is corrected for systematic errors created by differential reddening.

3.1 Identifying Matches

The `.xyms` files now need to be merged into catalogs. The first step uses `xym2mat`. This program requires an input file (`IN.xym2mat`) that describes information about and provides instructions for each image it needs to analyze.

Each line in `IN.xym2mat` gives a file number, file name, camera number, filter number, and magnitude range to analyze. The abbreviations for camera and filter number are specified within the program: c5 is the camera number for ACS/WFC, f4 is for F606W, and f5 is F814W. The first run includes all saturated stars, as this allows the program to identify matches more easily. The minimum magnitude is -11 (-9 for short exposures) and the maximum is -99. For example:

00 filename.xym c5 f4 ”m -99,-11”

01 filename.xym c5 f4 ”m -99,-11”

02 filename.xym c5 f4 ”m -99,-11” ...

The ”master frame” is the reference frame to which all other images from that filter and epoch will be matched. It is specified in the input file as file 00, and it should be the longest exposure. The numbering continues as 01, 02, etc. Later in the list, the master frame should appear again, numbered sequentially this time. The `xym2mat` program is executed in a folder containing `IN.xym2mat` and all the images. It takes one number as an argument that specifies the allowable difference between a star in the master frame and a star in another file to confirm a match (I used 15).

The master frame is compared to each image sequentially in a process called cross identification. Stars are sorted in terms of luminosity. The program begins from the brightest stars, identifying triangles in the images and searching for the same triangles in the master frame. A six parameter linear transformation is performed to translate each image into the coordinates of the master frame. This process creates files (called MAT files) corresponding to each image matched to the master frame. These files show the residual differences after the transformation. These residuals should be small and form a circle close to (0,0), as seen in Figure 3.1. The residuals between the master frame and itself are a point at zero.

Because the first run included saturated stars, the transformations are not of the highest quality. The `xym2mat` program needs to run again to refine the transformations it made the first time. The program automatically detects the presence of any existing MAT files in the folder, and uses them as a starting point when it is run any additional times. The second run is with saturated stars excluded, allowing the program to run faster and with better accuracy. New MAT files are generated each time, overwriting the old files. The maximum magnitude in this second iteration is -13.5, and the minimum magnitude is -10 (-8 for the long exposure).

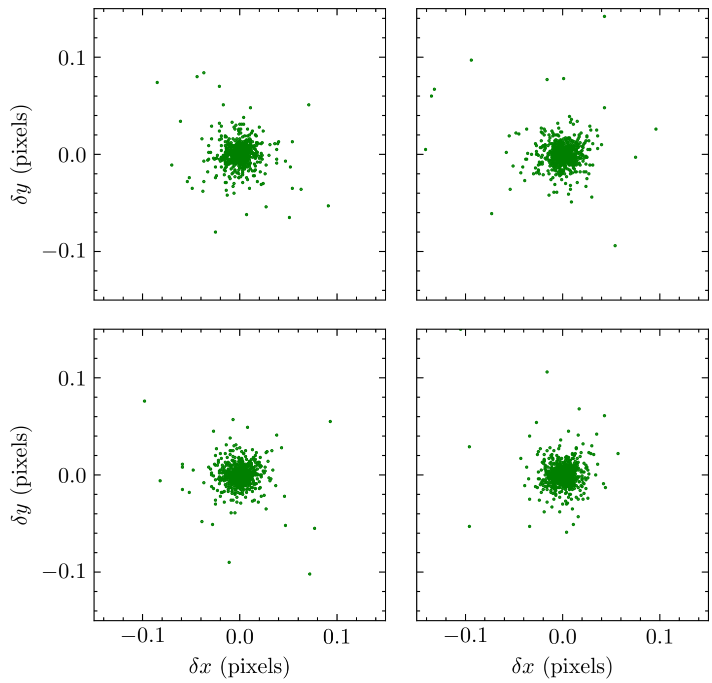

Figure 3.1: Four plots showing residuals from the cross identification process (F606W, 2005). The residuals form a small circle around the origin, indicating low error in the transformation.

00 filename.xym c5 f4 ”m -13.5,-10”

01 filename.xym c5 f4 ”m -13.5,-10”

02 filename.xym c5 f4 ”m -13.5,-10” ...

The final step to merge these files is running `xym2bar`. It averages the magnitudes of a star from different exposures to produce a final catalog. The program is executed in a folder containing the images that need to be combined, and an input file called `IN.xym2bar` which has a similar format to `IN.xym2mat`. In the long exposure images, I exclude stars that are saturated, and in the short exposures, I only include stars that would have been saturated in the long exposure. This made the magnitude range for long exposures from -13.5 to -4, and for short exposures from -99 to -9. In the long exposure, saturated stars have a magnitude of -13.5 Since we only want (long exposure) saturated stars to be measured in the short exposure image, we take the zeropoint difference between the master frame and a short exposure image and add that to -13.5, which gives -9.1 (use -9 to be

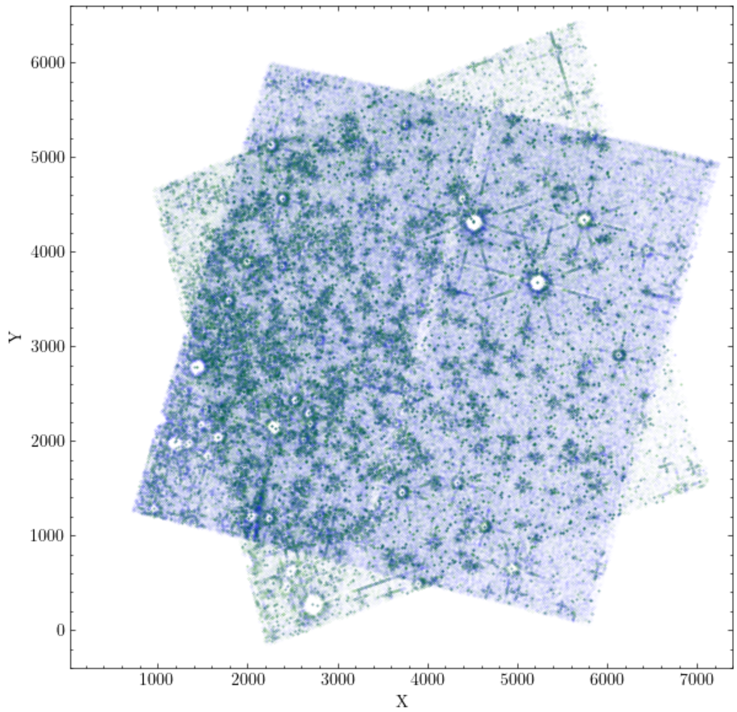

Figure 3.2: Stellar catalogs plotted in instrumental magnitudes to ensure the files were merged correctly.

conservative). The zeropoint difference can be found in `TRANS.xym2mat`, another output of `xym2mat`.

01 filename.xym c5 f5 "m-13.5,-4"

02 filename.xym c5 f5 "m-13.5,-4"

03 filename.xym c5 f5 "m-99,-9.0" ...

`xym2bar` takes as an argument the minimum number of files in which a star must be detected for inclusion in the final catalog (I used 2). The output file, `MATCHUP.XYMEEE`, contains many values, including positions in x and y, and magnitude.

To check that the `MATCHUP.XYMEEE` files have correctly translated all points into a common reference frame, I plot the corresponding files for F606W 2005, F606W 2006, F814W 2005, and F814W 2006. There do not appear to be any random outliers, which suggests a good match, and we can compare Figures 2.1 and 3.2 to see that the two epochs appear to be oriented properly in relation to each other.

3.2 Gaia Coordinates

The images have all been merged into single reference frames, but the coordinate system is arbitrary and based on the instrumental coordinates of the CCD. The coordinate system needs to be translated into right ascension and declination. To do so, I match the `MATCHUP.XYMEEE` file from F814W (2006) to `GAIA.XY`, which contains coordinates and magnitudes obtained from *GAIA* Data Release 3 [Prusti et al., 2016, Vallenari et al., 2023] for the same field. Using `xym1mat`, I link `GAIA.XY` to `MATCHUP.XYMEEE`. This is done in two parts: first using a magnitude range limited to only the brightest stars, and then a second run for all stars. Doing this process in two iterations allows the program to use the initial match from the limited range to process the second, more in depth iteration faster. This program generates a file linking all the stars from the *GAIA* catalog to matching stars in the F814W catalog, with position and magnitude in *GAIA* magnitudes and F814W magnitudes.

To obtain a file with a final catalog, I repeat the process from Section 3.1 to transform the F814W (2006) images into one catalog, and transform that catalog into the reference frame of the new file linked to *GAIA*. A master frame was generated from the linked file and used in `IN.xym2mat`, and the old `MAT` files were moved to a different directory so that they could not be used as a reference by the program. Finally, the `IN.xym2bar` program creates the final catalog. For the other 2006 epoch, this process is repeated using the final catalog from F814W (2006). For the 2005 epoch, since I already have the magnitude calibration completed in each filter, I only need to do the reference calibration (process from Section 3.1).

3.3 Photometric Calibration

At this point, the magnitudes of stars in the catalogs are in terms of instrumental magnitude. They need to be converted into a common magnitude reference system, so that the results can be compared to the literature. There are three elements to account for in order to correct the magnitudes: exposure time, aperture size, and zeropoint. The zeropoint is a value that is specific to an instrument: it corresponds to the magnitude that registers one count per second. This value is calculated and provided by the Space Telescope Science Institute (StSci) on

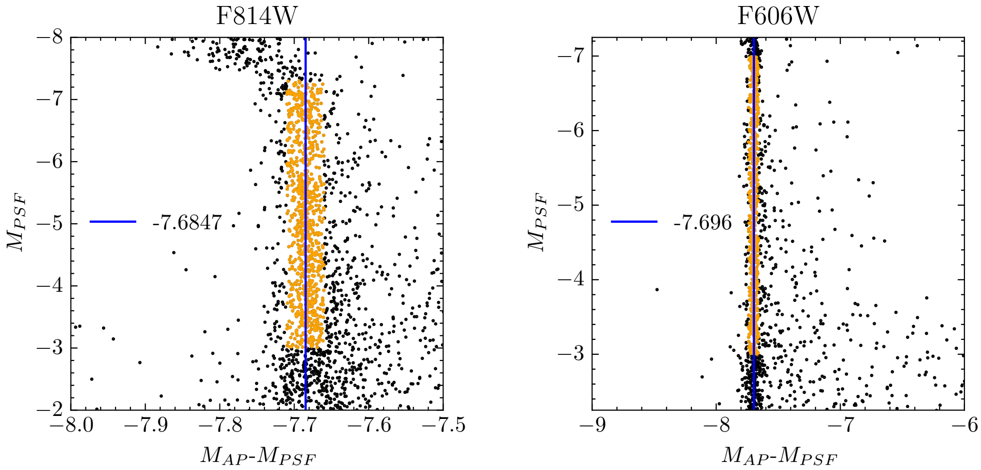

Figure 3.3: The median values correspond to the photometric zeropoint of an image with the standard exposure time.

specific dates for each instrument and filter.

1.) Exposure Time

The instrumental magnitude of each star in each image depends heavily on the exposure time. The effects of detector efficiency and pixel size are also taken into account in this step. To do this, we analyze the *drc.fits files mentioned in Section 2.2. These images are drizzled, which means they are stacked from all the exposures in each given year and filter, with all cosmic rays, artifacts, etc. removed. Although some information is lost because the pixels are stacked together, this is taken into account because the drc image is properly normalized to one second exposure time. That means that the photometric zeropoint of this image corresponds to the zeropoint of an image with standard exposure time. This value is used to remove the dependence on exposure time from the master frame.

To find the values to use for this dataset, I perform aperture photometry on the *drc.fits image. I use the program `drz_phot_gfortran.e`, which takes 4 arguments + the name of the *drc.fits file:

- minimum distance between two stars to be measured (10)
- minimum flux to be considered a star (0.1)

- maximum flux to be considered a star (9999)
- a phrase with specifications for aperture photometry (10 (radius of aperture), 14) inner radius), 20 (outer radius))
- filename_drc.fits

Next, I compare this photometry to the catalogs created in Section 3.2. The first step matches the `.xym` output from this process to those catalogs (procedure in Section 3.1, now referred to as PSF magnitudes). Then I make a plot of PSF magnitudes minus aperture magnitudes as a function of PSF magnitudes. After removing saturated stars, those which are clearly too faint, and any outliers, that which remains will form a vertical column corresponding to the photometric zeropoint difference. I take this value as the median value of the column (see Figure 3.3). The PSF photometry differs from the aperture photometry by this amount on average, due to exposure time, detector efficiency, and pixel-level effects. It will be added to the magnitude to find the calibrated magnitude values.

2.) Aperture Size

The light from each star is not confined to a perfectly sized area to measure. In fact, due to the diffraction of light when it is measured by the CCD, some of the light from the star is always lost because the full Airy disk cannot be measured. To account for this, StSci provides Encircled Energy (EE) Tables[1] [Bohlin, 2016] with calculated values for ACS/WFC in each filter for different pixel radii (I used 10px). These values are 0.914 for F814W and 0.916 for F606W and are added to the final value as $-2.5\log(EE)$.

3.) Zeropoint

ACS/WFC	VEGAmag	F606W	2006-11-09:	26.400
ACS/WFC	VEGAmag	F814W	2006-11-09:	25.500

Finally, I add values from the ACS Zeropoints calculator from StSci[2] for the dates on which the observations were made, to convert the magnitudes into the VEGAmag system.

[1] https://www.stsci.edu/hst/instrumentation/acs/data-analysis/aperture-corrections

[2] https://acszeropoints.stsci.edu/

$$\text{F814W}: \; 7.685 + 25.5 - 2.5\log(0.914) = 33.2826$$

$$\text{F606W}: \; 7.696 + 26.4 - 2.5\log(0.916) = 34.1913$$

After these corrections are applied to the magnitude, I can create an initial CMD.

3.4 Differential Reddening Correction

Light coming from distant stars is scattered by dust that exists in the interstellar medium between the stars and Earth. Light at higher wavelengths is scattered more efficiently than at lower wavelengths. This causes light received from areas with significant amounts of dust in front of them to appear much redder than they actually are. This effect, reddening, needs to be corrected for in order to find accurate magnitude measurements.

The absorption $A_\lambda = m_\lambda - m_0$ is the difference between the observed and intrinsic magnitude of a star, and it quantifies the amount of reddening at a specific wavelength. To compare the absorption at two different wavelengths, we calculate the color excess:

$$E(B-V) = (B-V)_{obs} - (B-V)_0 \tag{3.1}$$

This is traditionally done using the B and V bands of the UVBRI (Johnson-Kron-Cousins) system. It can be related to the absorption as follows:

$$A_\lambda = k_\lambda E(B-V). \tag{3.2}$$

To find the final corrected magnitude of the star, I take the magnitude calculated in Section 3.3 and subtract A_λ. Different values of k_λ are used for different filters, and those specific to HST filters can be found online. I used $k_{F606W} = 2.8782$ and $k_{F814W} = 1.8420$.

When correcting for reddening, it is important to consider that it may not be the same in all directions, even from one side of a cluster to another. This is called differential reddening. Differential reddening can be calculated directionally and applied as a correction to stars individually, allowing for more accurate pho-

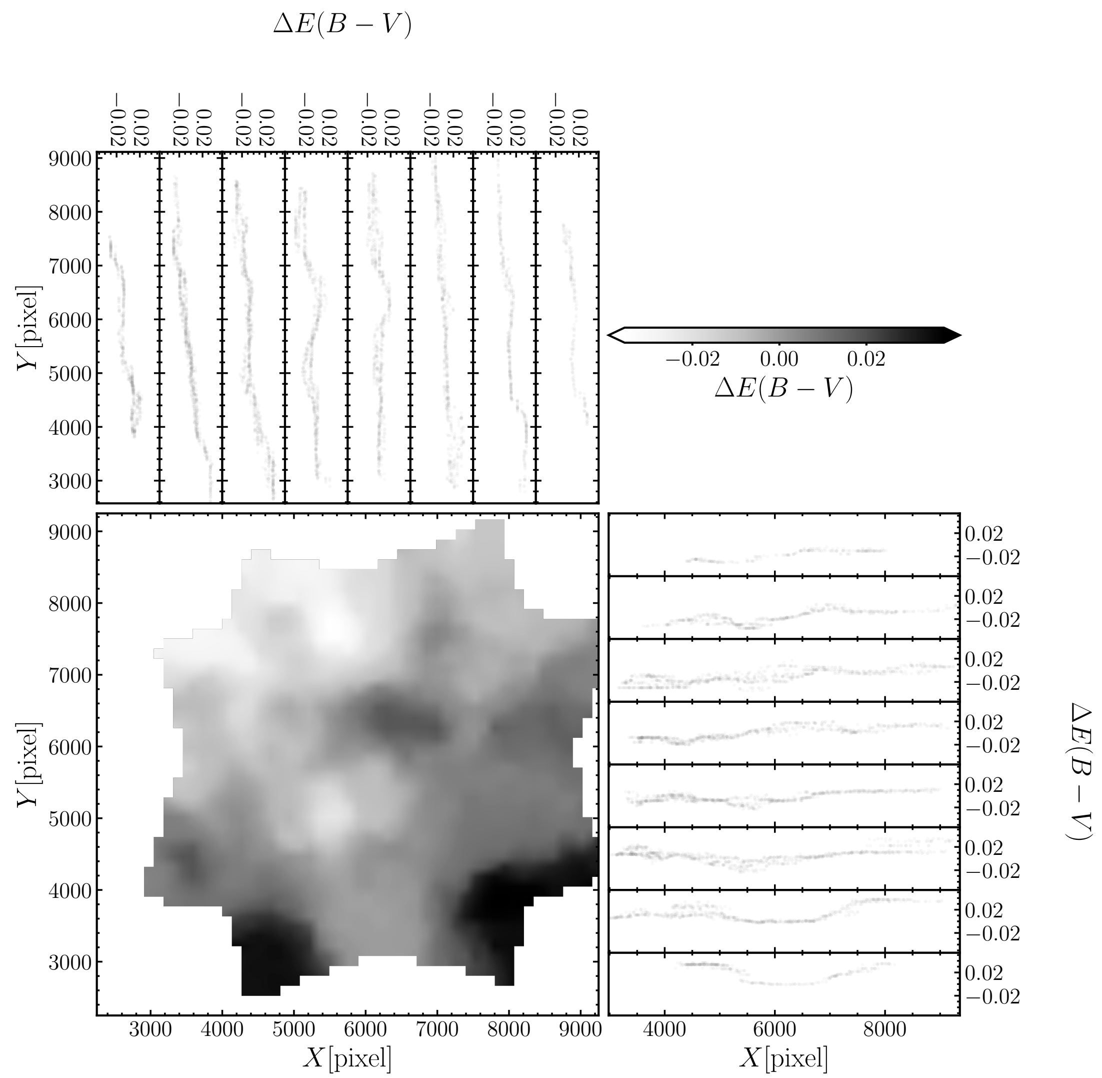

Figure 3.4: Differential reddening across NGC 2158.

tometry. The process for calculating reddening for different parts of the cluster involves an iterative method. Reference stars are selected such that the reddening direction is at a wide angle with respect to the fiducial line. This makes it easier to separate photometric effects from change in color and magnitude due to differential reddening. The reddening direction for each reference star is derived as an angle $\theta = \arctan \frac{A_X}{A_X - A_Y}$, in which A_X and A_Y are absorption coefficients in the two bands used for the CMD. These values are found using the isochrone. The corresponding point is found on an isochrone for which $E(B-V) = 0$. Then, the CMD and fiducial line are translated into a new reference frame by an angle θ such that the reddening direction is vertical. The distance of the reference stars from the fiducial line are found along the reddening direction, and this is used to quantify the amount of reddening in different areas. When finding the differential reddening for each star, a sample of N nearby stars is selected. The median $\Delta E(B-V)$ value of these stars is taken as the best determination for the selected star.

Functionally, this correction is applied to magnitude values as a unique $E(B-V)$ value for each star, using equation 3.2. Figure 3.4 shows differential reddening across NGC 2158. The code for this differential reddening visualization was provided courtesy of M.V. Legnardi. The field of view is split into 8 horizontal and vertical strips to show variations as a function of the horizontal and vertical axes. Darker gray indicates a higher amount of reddening in that area.

Figure 3.5 is a portion of the CMD of NGC 2158, showing the corrected points in black on top of the reddened points in red, showing a tighter main sequence and binary sequence and an overall improvement in photometry.

3.5 Second Pass Photometry

The second step of photometry, which calculates among other things the differential reddening values (3.4), is calculated using the KS2 program. The first pass of photometry described previously is best-suited for the brighter stars, and this pass refines values for fainter stars. A feature of this program is that it operates iteratively on the images, by first measuring the brightest stars and then subtracting them. This process is repeated and measures fainter and fainter stars to eventually derive magnitudes and positions for all sources. The first pass acts as

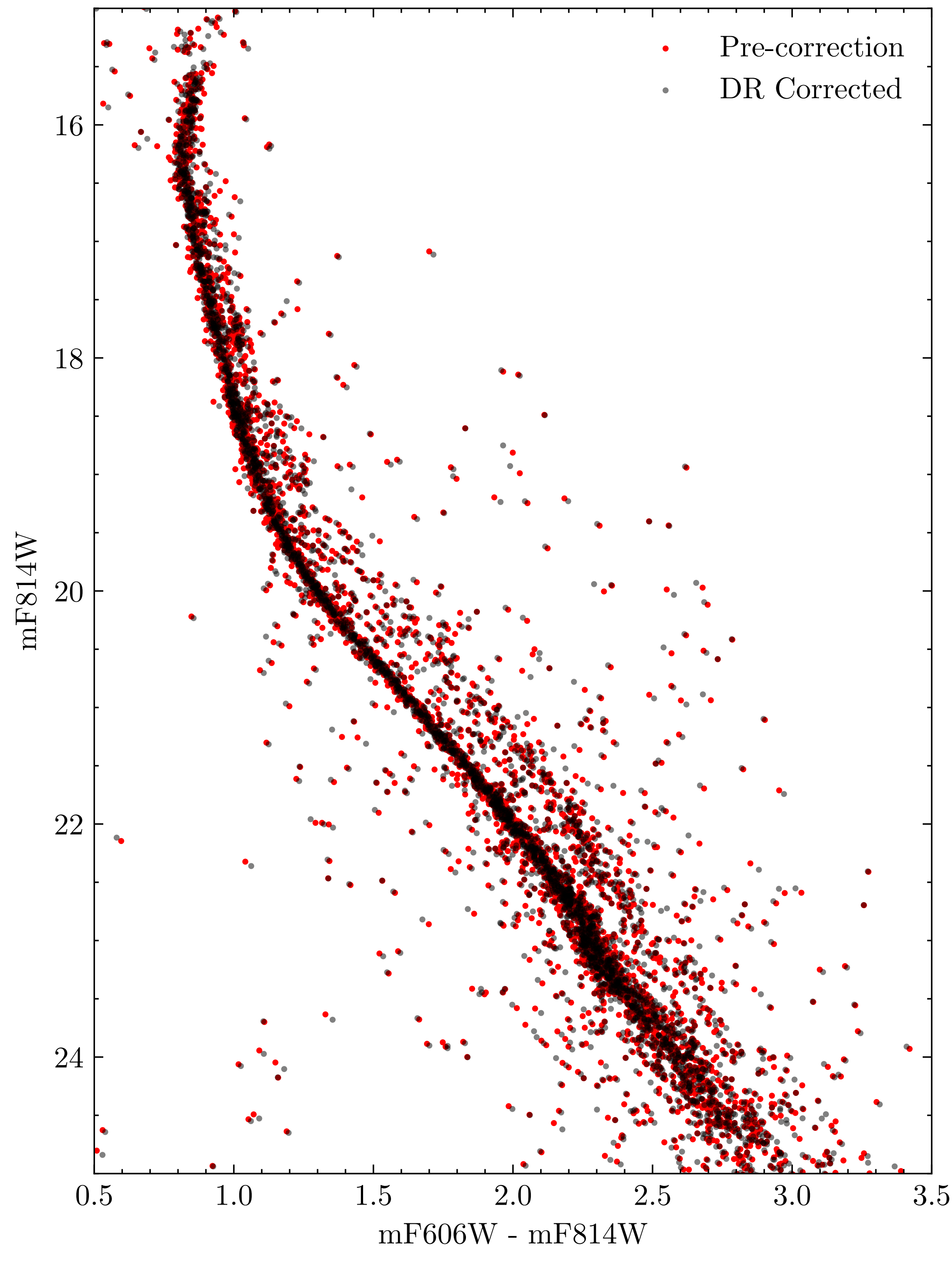

Figure 3.5: Differential reddening correction, shown on a portion of the NGC 2158 CMD. Red points are reddened, black points are corrected.

a starting point, allowing this pass to be as accurate as possible.

The program uses three different methods so that ultimately all stars are well measured. The first method for bright stars uses the PSF model from the first pass. The second method targets fainter stars that were not well measured by the PSF (see Fig. 2.3), performing aperture photometry. The third method is used for very crowded regions. It can also be used for faint stars that are visible in many exposures. This method uses a slightly altered aperture photometry method from the previous, with a smaller inner radius and an annulus further from the star. It was not used, as this cluster is not a particularly crowded region and so the results are worse with this method. As in the first pass, the position and flux determinations are merged together to find a final catalog, and calibrated.

As part of this pass, an artificial star test is performed. It individually simulates a number of single stars much greater than the observed number of stars in the cluster, and measures them using the same data reduction process to have comparable values. These stars should replicate the same characteristics of real stars. The artificial stars are generated with a flat luminosity function and inserted into an image. If, after the reduction process, the measurement of the simulated star finds that the position is within 0.5 pixels and the flux differs by less than 0.75 mag, it is considered "found." Since these are all single stars, this analysis lets us estimate how many of the measured binaries in a cluster are not binaries, but in fact chance superpositions of single stars (see Section 4.2).

Also important to the analysis is the completeness. Completeness is a measure of how many stars "exist" vs. how many of the existing stars are "found." First, the field is split into concentric rings centered on the center of the cluster, and the stars within each ring split into magnitude bins. By finding the ratio of "found" to "existing" stars in each bin, we can find the average completeness and use this to estimate the completeness for every star in the cluster [Milone et al., 2009]. As a rule, portions of the CMD with low completeness (generally, below 50%. see Figure 3.6) are considered unreliable and typically excluded from the main analysis.

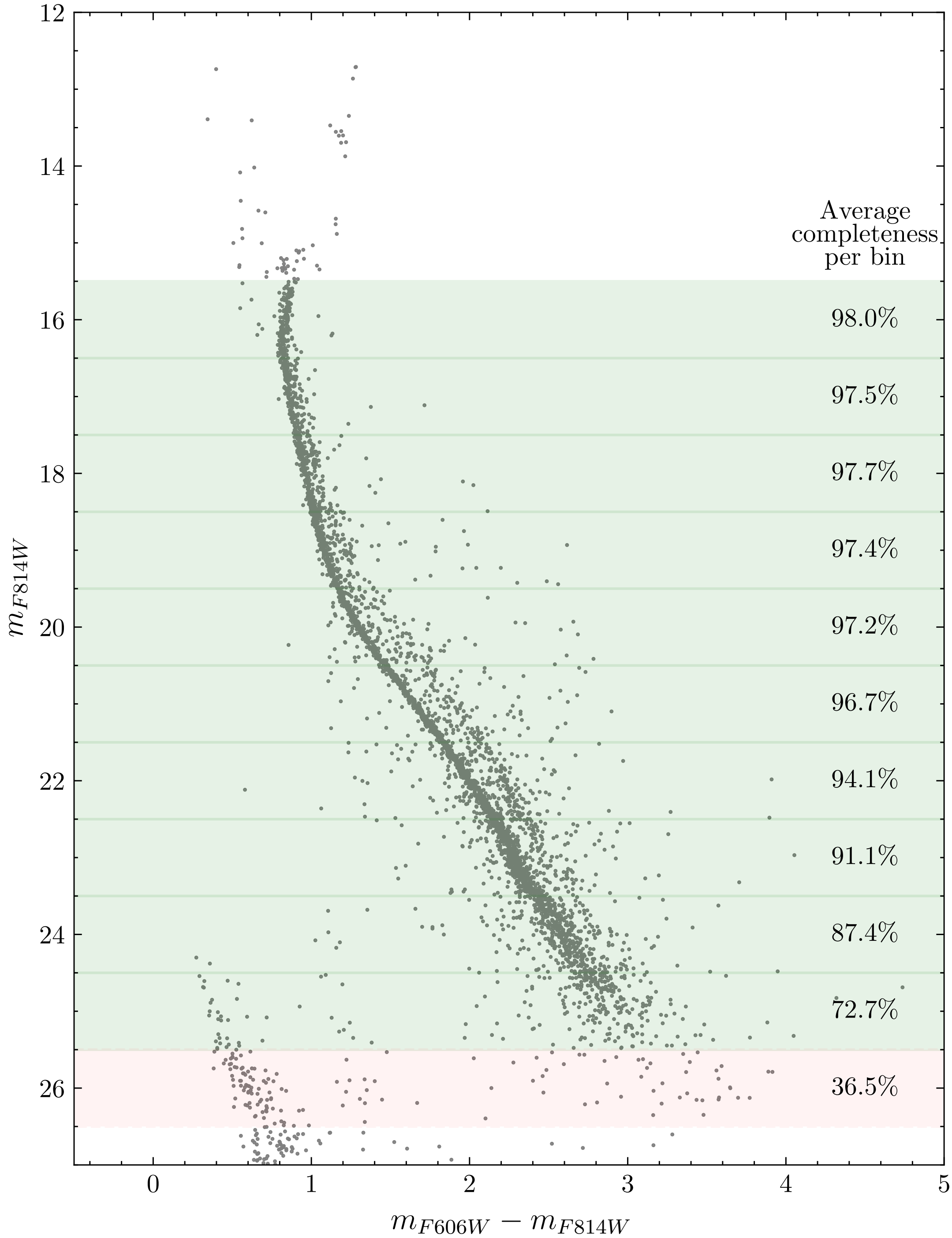

Figure 3.6: Average completeness value per bin. The ten bins used for mass and luminosity function analysis are those with completeness above 50%, shown in green. The final bin has an average completeness of only 36.5% and was therefore excluded from analysis.

4

Results and Discussion

With the photometric corrections applied, I can proceed with the data analysis. I choose an isochrone and create a fiducial line, both of which are used in the calculation of the binary fraction. The binary fraction is compared at $q = 0.6$ to the open clusters in Cordoni et al. [2023] and the Small Magellanic Cloud (SMC) field. I then find the luminosity function and mass function, after accounting for completeness. The α values for the mass function, as well as the stellar mass region explored, are compared to other mass functions.

4.1 Color-Magnitude Diagram

The first result after creating a stellar catalog is the CMD, shown in Figure 4.1. This CMD of NGC 2158 is plotted as $mF814W$ against $mF606W - mF814W$, and extends from above the main sequence turn off down to masses of approximately $0.1 M_{\odot}$. To the left of the main sequence turn off, there appear to be multiple blue straggler stars. This CMD shows a clear binary sequence parallel to the main sequence.

Isochrones are curves of stars that have the same age, chemical composition, and distance. To fit the isochrone, I consulted previous results from the literature before selecting by hand the best fit. A high resolution spectroscopic analysis of NGC 2158 by Jacobson et al. [2009] determined the metallicity at [Fe/H] = -0.03 ±

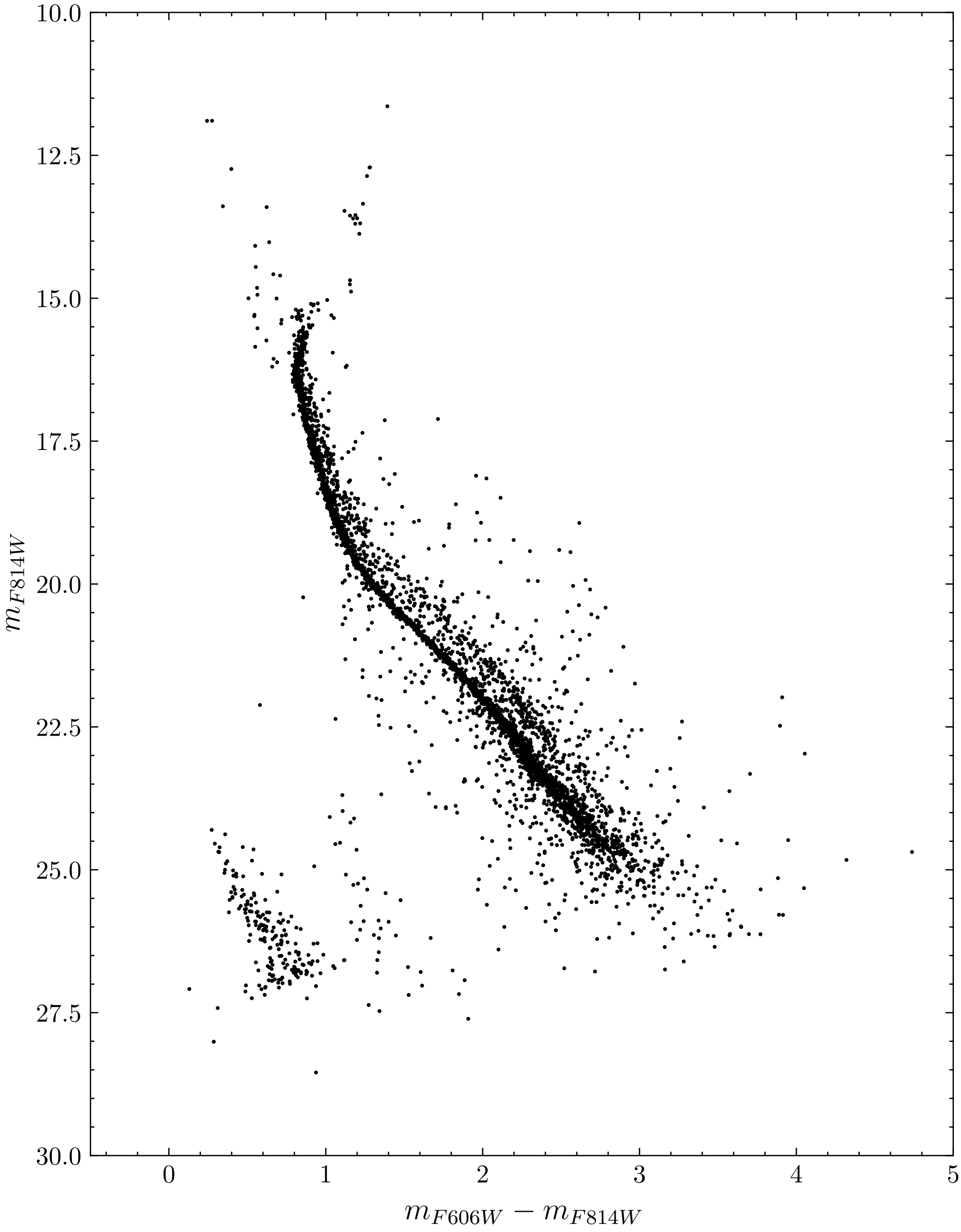

Figure 4.1: Color magnitude diagram of NGC 2158, $mF814W$ vs. $mF606W - mF814W$.

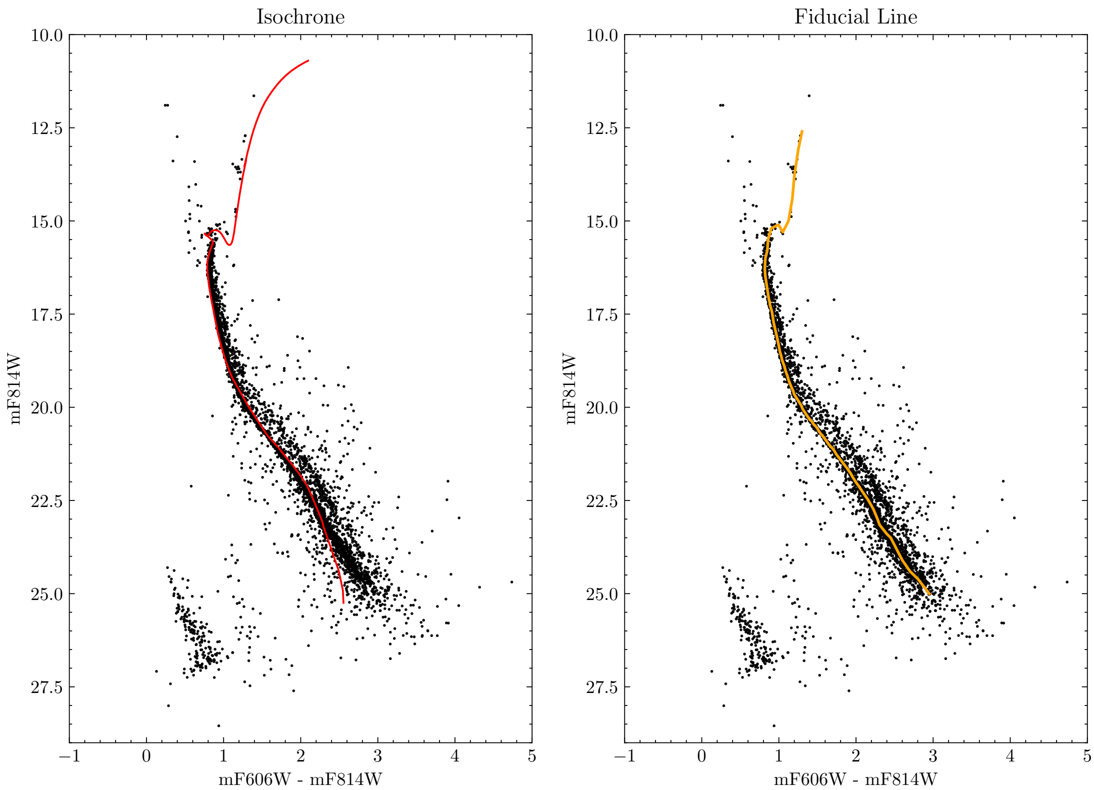

Figure 4.2: Left: isochrone of NGC 2158: [Fe/H] = -0.03, 1.9 Gyr. Right: fiducial line for NGC 2158.

0.14. The age is accepted as between ~ 1.8 to ~ 2 Gyr [Sariya et al., 2021, Bedin et al., 2009, Carraro et al., 2002]. Additionally, I used the distance of $4770pc$, as given in the Kharchenko, N. V. et al. [2013] catalog. The E(B-V) value of 0.4373 is from the Infrared Science Archive [IRSA, 2022][1] and in agreement with Carraro et al. [2002], and was used in the initial fitting of the isochrone. Once differential reddening was calculated for the stars in the cluster, the corrections were applied individually as described in Section 3.4.

Considering these values, I found the best fit isochrone to be [Fe/H] = -0.03, with an age of 1.9 Gyr, which is plotted over the CMD in the left panel of Figure 4.2. The isochrone is from the Dartmouth Stellar Evolution Database [Dotter et al., 2008][2].

To create the fiducial line, that represents the cluster's main sequence, I divided

[1] https://irsa.ipac.caltech.edu/applications/DUST/
[2] http://stellar.dartmouth.edu/~models/

the CMD into bins and found the median color and average magnitude for each bin. I used a boxcar binning method, in which I took bins of 0.5 magnitude, found the median color and average magnitude of stars in the bin, and then shifted the bin down by 0.1 magnitude. I repeated the process until I sampled the entire main sequence. In this way, while there are more points and they are not completely independent of each other, the fiducial line better samples the PSF variation. For magnitudes above the main sequence turn off, I selected points by hand in order to have a complete fiducial line, because the data above the turn off point is not being used in this analysis and has higher error. The fiducial line is plotted over the CMD in the right panel of Figure 4.2.

4.2 Binary Fraction

I calculated the binary fraction for the main sequence of NGC 2158 from 17.5 magnitudes to 24.5 magnitudes (F814W), and then separately in bins of one magnitude to see how the fraction varies with stellar mass. To do this, I used a SuperMongo macro provided by Prof. Milone, which calculates the binary fraction for a given magnitude range. As shown in Figure 4.3, it selects a portion of the main sequence between the two blue lines that corresponds to the given magnitude range. The blue lines are curved to account for the way the light from a binary system of a certain mass ratio blends and changes the observed magnitude (Figure 1.1). Region A (top left) consists of all the stars in the selected magnitude range, and Region B (top right) is the region containing binary stars at or above the selected mass ratio, q, unrelated to the q value for quality fit from the data reduction process. Stars in Region A but not B are shown in black, and those in B are shown in red. The solid green line is the isochrone, which is important to the binary fraction calculation, because it is used to associate a mass to each star. The solid red line delineates the separation between main sequence stars and binaries.

When calculating the binary fraction, it is important to account for potential false binaries. Observational errors can push the value of a star's magnitude into the binary region, or a blend of two stars superimposed can create a fake binary. We can estimate this contamination using an artificial star analysis. The artificial stars are run through the same data reduction process as the observed stars,

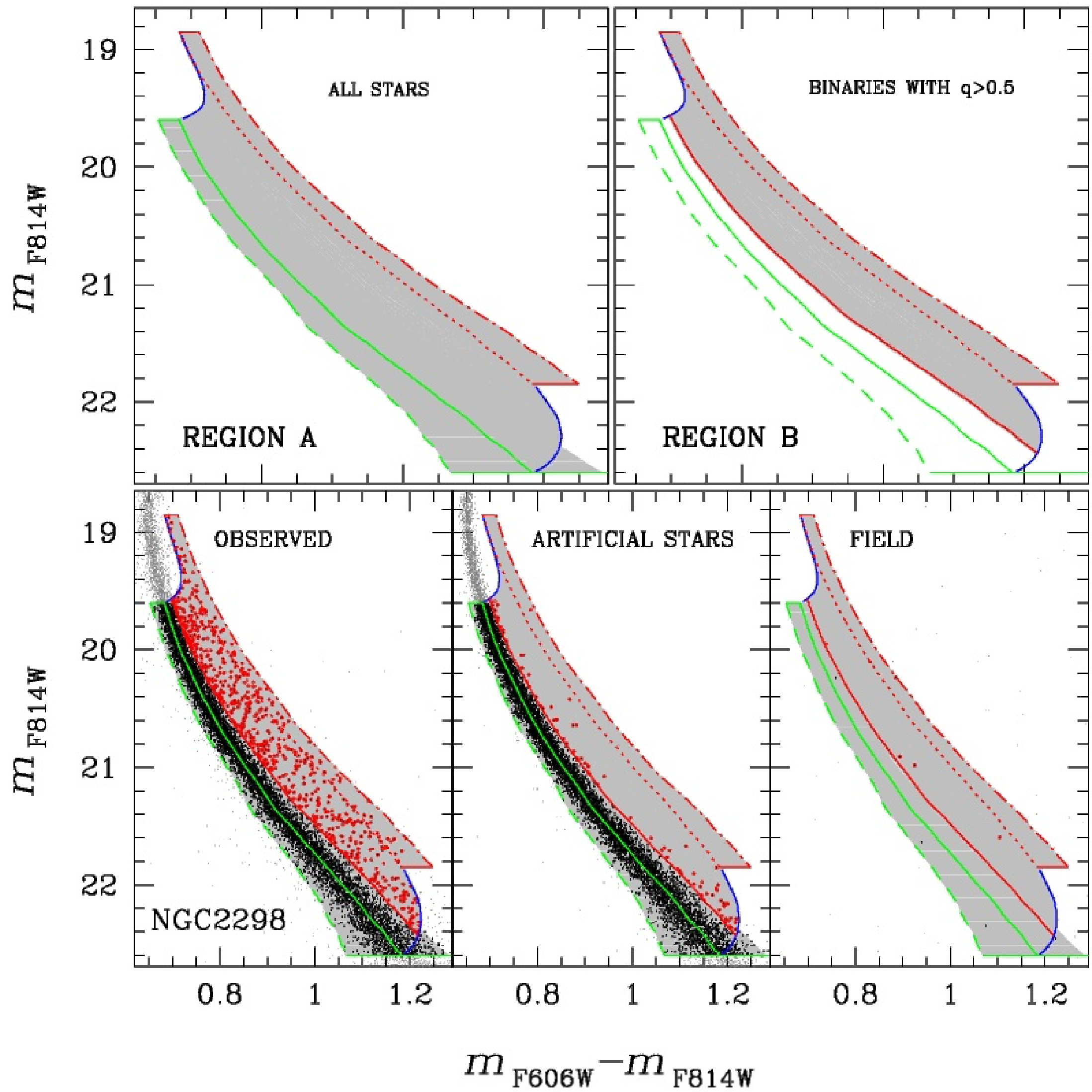

Figure 4.3: Adapted from Milone et al. [2012], this figure shows regions A containing all stars, and B containing only binaries, as it is used in binary fraction calculations, here for NGC 2298 with observed, artificial, and field stars.

and then through the same binary fraction analysis, in order to find comparable results. Two single stars may be at positions close enough to each other to blend and simulate a binary, and one of the goals of this artificial star test is to find how many false binaries are measured in a given region [Milone et al., 2012].

The two epochs of observation are too close to each other to provide a long enough temporal baseline that can be used to completely separate field star contamination. Therefore, we simulate the field using the TRILEGAL[3] program, specifying the cluster coordinates and instrument (ACS/WFC). This program simulates photometry of the Galactic field in a given region [Girardi et al., 2005]. By putting this data through the same binary fraction calculation, we can find and remove the field contamination.

The binary fraction f_B is described in equation 4.1.

- N^A and N^B are the number of stars in regions A and B for each type of star (observed (obs), artificial(AS), field)
- Normalization factor $f_{norm} = A_{ACS}/1\ \text{deg}^2$ normalizes the field star region to the correct size (A_{ACS} is the area of the ACS/WFC instrument, which is ~ 202 arcsec per side)

An example of this process can be seen in the bottom three panels of Figure 4.3, where for artificial and field stars we can see that some fall into the range of binary detection despite not being binaries themselves. In this way we can remove them accurately from our star counts.

$$f_B = \frac{(N^B_{obs}) - (N^B_{field} \times f_{norm})}{(N^A_{obs}) - (N^A_{field} \times f_{norm})} - \frac{N^B_{AS}}{N^A_{AS}} \tag{4.1}$$

For a mass ratio $q = 0.5$, the binary fraction for the full main sequence is $f_{bin} = 0.19$. I calculated the binary fraction for $q = 0.5, 0.6, 0.7$ in bins of one magnitude to examine how the fraction changes with respect to stellar mass (luminosity). It is clear from Figure 4.4 that as the stellar mass decreases, the binary fraction decreases. This is consistent through all three mass ratios investigated. Milone et al. [2012] found that the binary fraction remains flat with decreasing stellar

[3] https://stev.oapd.inaf.it/cgi-bin/trilegal

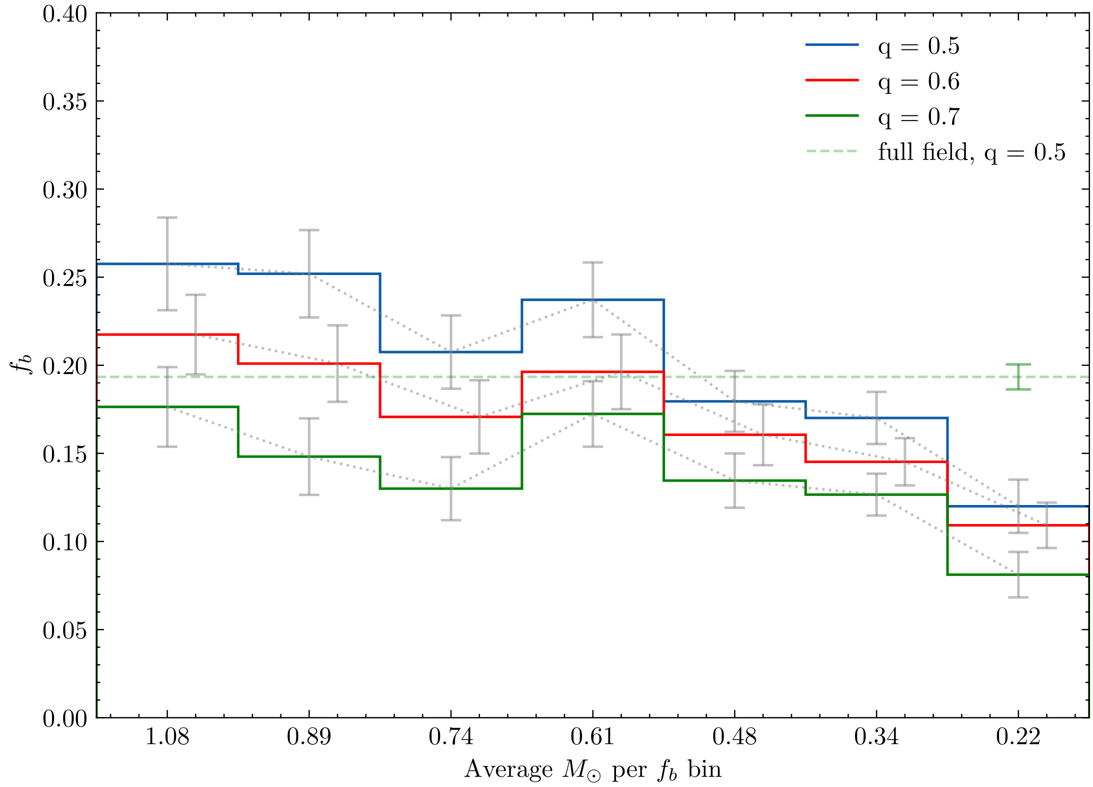

Figure 4.4: Binary fraction in bins of 1 magnitude for three mass ratios. As the stars become fainter and less massive, the binary fraction decreases.

mass for most of the 59 globular clusters in that study. For most clusters in that work, the main sequence is split into three bins of one magnitude, from 0.75 to 3.75 magnitudes in F814W below the main sequence turnoff. In this work, the main sequence below the turn off point is split into seven bins of one magnitude, from 17.5 to 24.5 magnitudes in F814W. It shows a clear decrease in the binary fraction at very low masses. The ability to split NGC 2158 into seven bins of one magnitude as opposed to three bins of one magnitude likely contributes as well. Cordoni et al. [2023] also finds no decrease in binary fraction with stellar mass, but the mass range is limited to around $0.4M_\odot$ depending on the cluster, which is enough to reveal a difference.

In Figure 4.5 (a), the full main sequence binary fraction of NGC 2158 at $q = 0.6$ (blue square) is compared to the open clusters studied in Cordoni et al. [2023] (green x markers), and to the value of the field for the SMC from Legnardi et al.

[2025]. (orange diamond). We can see that the value of the binary fraction is on the higher and older end, but in the same range as other open clusters studied in Cordoni et al. [2023]. The ages for the other open clusters are from Dias et al. [2021].

In (b), the gray dots represent binary fractions by stellar mass in the Galactic field from Offner et al. [2023] and references therein, blue squares NGC 2158, and the orange diamond is again the SMC field. The binary fraction in the Galactic field decreases with stellar mass, which is also seen in the binary fraction of NGC 2158. This is interesting, because while this binary fraction trend has been found in the Galactic field, previous studies that analyzed clusters found no significant decrease in binary fraction with stellar mass. While it is possible that the different environments of the Milky Way field vs. open/globular clusters affect binary evolution, it is likely that this difference is due to the limited mass range of previous studies ($\sim 0.4 - 0.5 M_{\odot}$). While the fractions in NGC 2158 are somewhat higher than the values for the field, they clearly show the same downward trend. The formatted data for the open clusters, Galactic field, and SMC field, along with the visualization for Figure 4.5, were provided courtesy of M.V. Legnardi [Legnardi et al., 2025].

4.3 Luminosity and Mass Functions

The luminosity and mass functions begin with the number of stars per magnitude interval (Figure 4.6). As part of the artificial star analysis, we also find the completeness, which relates the number of stars observed to the true (or complete) number of stars in the cluster. As detailed further in Milone et al. [2009], a completeness value is calculated for each star. For each magnitude interval, I calculated the number of stars and corrected for completeness by multiplying the number of stars by the completeness values,

$$N_{complete} = \sum_{1}^{N_{init}} \frac{1}{c_i} \tag{4.2}$$

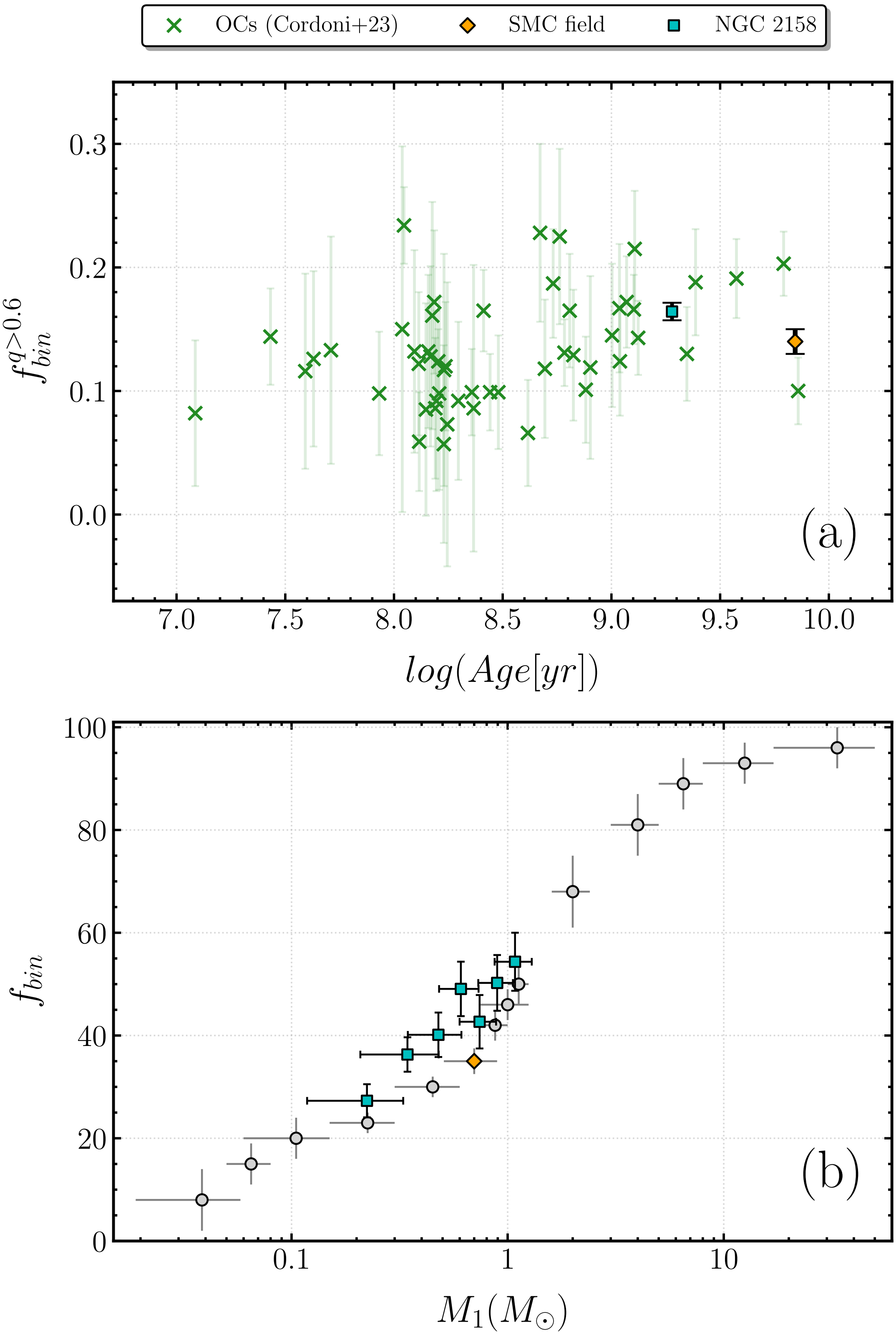

Figure 4.5: (a) NGC 2158 binary fraction in comparison to other open clusters, and the SMC field. (b) Galactic field (gray dots), SMC field (orange diamond), and NGC 2158 (blue squares) binary fractions against stellar mass, showing clear relation between stellar mass and binary fraction.

in which c_i is the completeness for each respective star. This number is then adjusted for the binary fraction.

$$N_{final} = N_{complete} + N_{complete} \times f_{bin} \tag{4.3}$$

To find the value for the luminosity function, I divide N_{final} by the difference in magnitude Δm of the bin. The y axis is represented as the log of this value.

For the mass function, the process is similar. After finding N_{final}, I use the isochrone to interpolate linearly the given magnitude and stellar mass values (all in terms of $M_\odot$) in order to easily relate a given magnitude to a given mass. I find ΔM, and calculate the value for the mass function by dividing $N_{final}/\Delta M$. To represent the average stellar mass per bin in Figure 4.6, I take the average magnitude of the stars in the bin and convert it to stellar mass.

The error calculation for each bin is represented through Poissonian counting error corrected for the log representation of the y axis.

$$\begin{aligned} \sigma_{upper} &= \log\left(\frac{N+\sqrt{N}}{\Delta m}\right) - \log\left(\frac{N}{\Delta m}\right) \\ \sigma_{lower} &= \log\left(\frac{N}{\Delta m}\right) - \log\left(\frac{N-\sqrt{N}}{\Delta m}\right) \end{aligned} \tag{4.4}$$

This analysis of NGC 2158 explores the deepest mass range to date. From Figure 4.8 we can see that it has clear changes in slope at $\log(M/M_\odot) \approx -0.05$ and -0.3. To find α, the slope of the mass function, I fit each segment using a linear regression method. The best fit slopes left to right are $\alpha \approx 2.27$, $\alpha \approx -1.24$, and $\alpha \approx 0.03$. This is plotted with other mass functions in Figure 4.9. The change in slope around $\log(M/M_\odot) \approx -0.3$ is consistent with expectations for a Kroupa-like mass function. The change in slope at $\log(M/M_\odot) \approx -0.05$ is in agreement with the open clusters studied in Cordoni et al. [2023], which overall show a change in α at approximately -0.05, or $\sim 1M_\odot$, not $\sim 0.5M_\odot$ as would be expected for a Kroupa mass function. The mass functions in Cordoni et al. [2023] are split into a low-mass and high-mass range, splitting at $\sim 1M_\odot$. Since this study extends the analysis of the mass function much further to ~ -0.85 (compared to -0.35), we can divide the mass function in Figure 4.8 into three

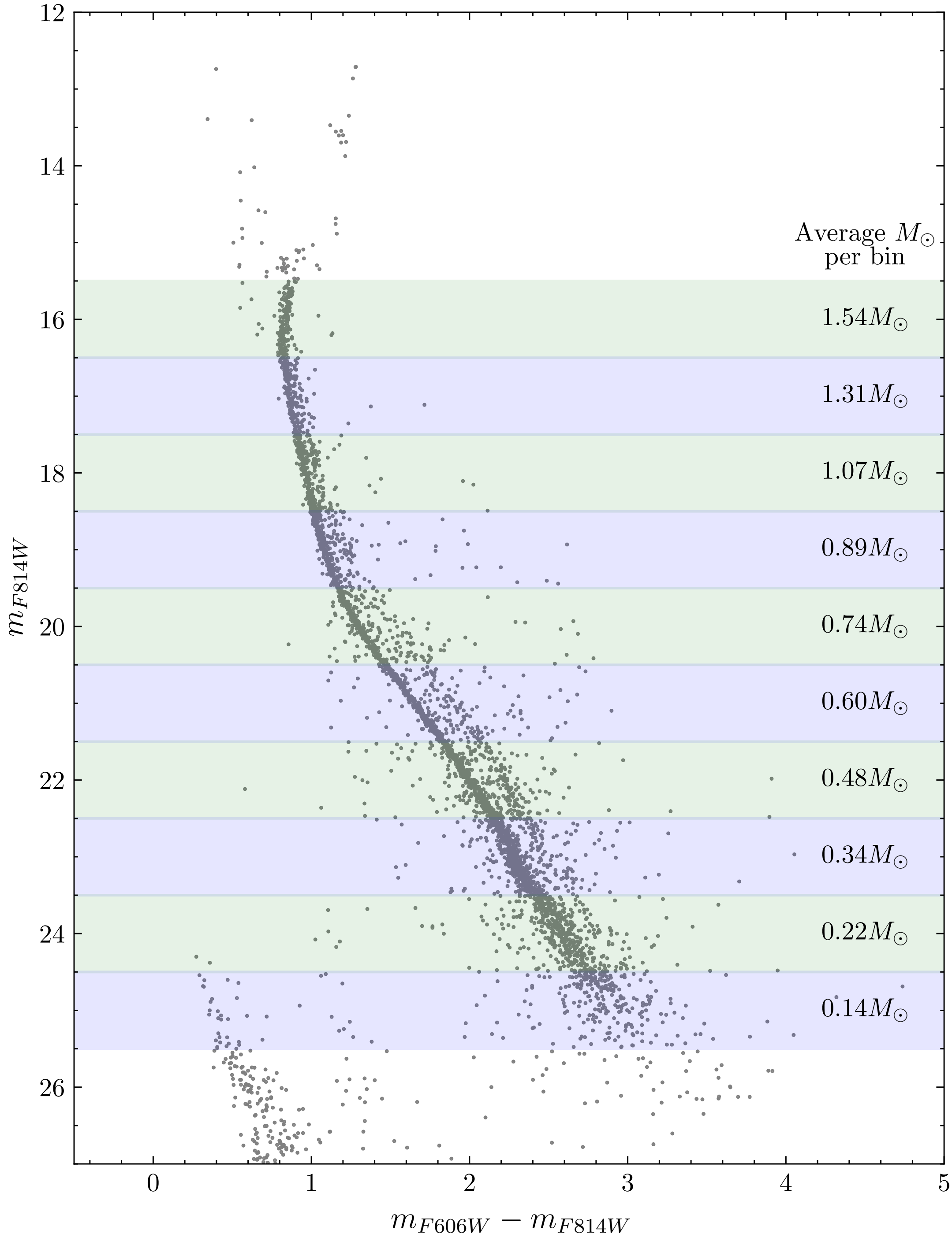

Figure 4.6: Bins used for the luminosity and mass functions, with the average stellar mass ($M_\odot$) per bin.

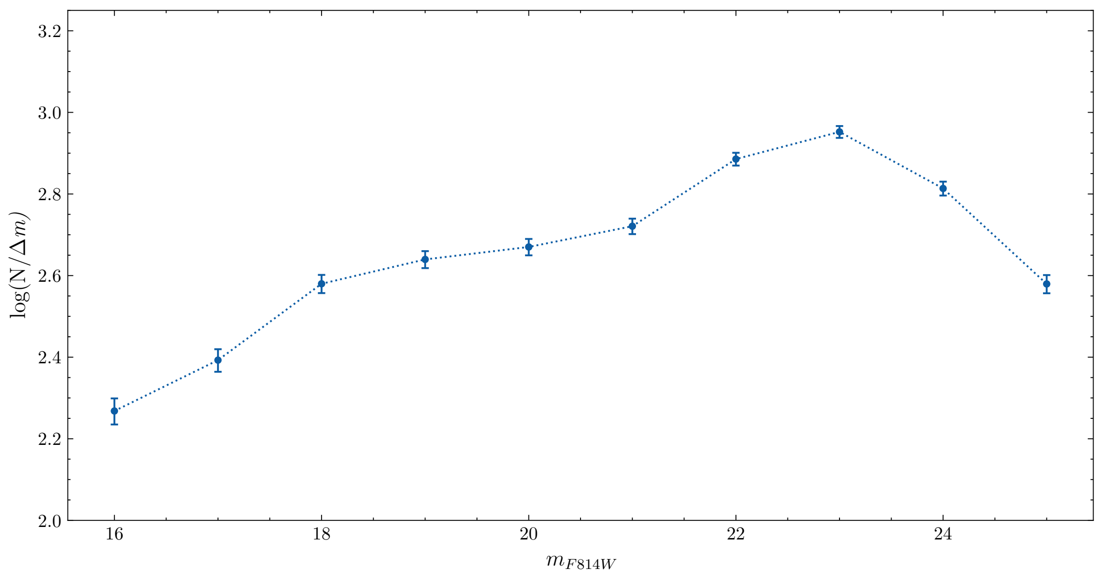

Figure 4.7: Luminosity function for NGC 2158.

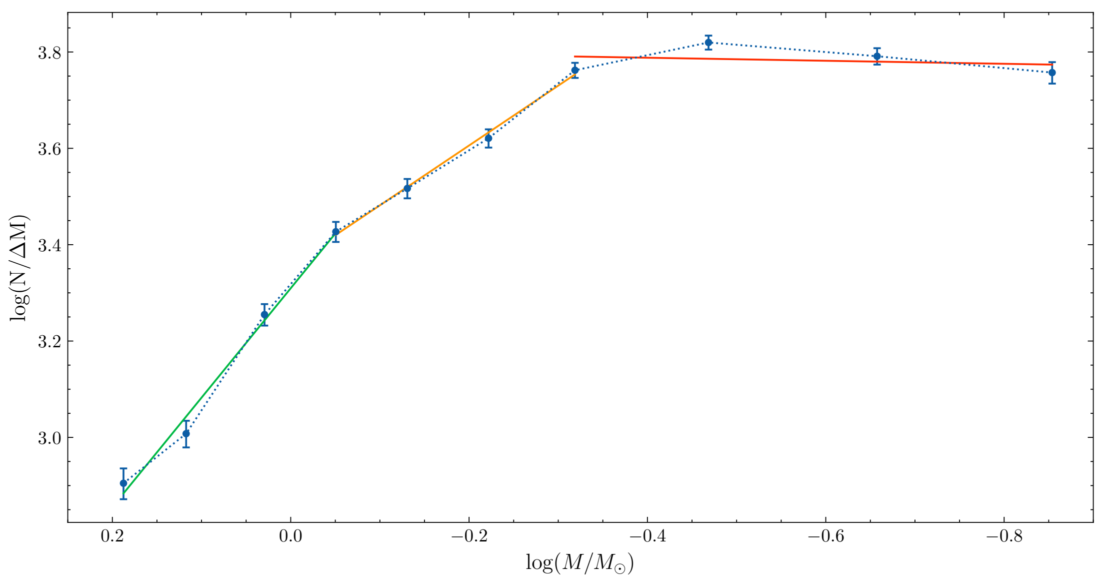

Figure 4.8: Mass function for NGC 2158. Lines of best fit for slope are plotted for three regimes: $\alpha = -2.27$ for high mass, $\alpha = -1.24$ for low mass, and $\alpha = 0.03$ for very low mass stars.

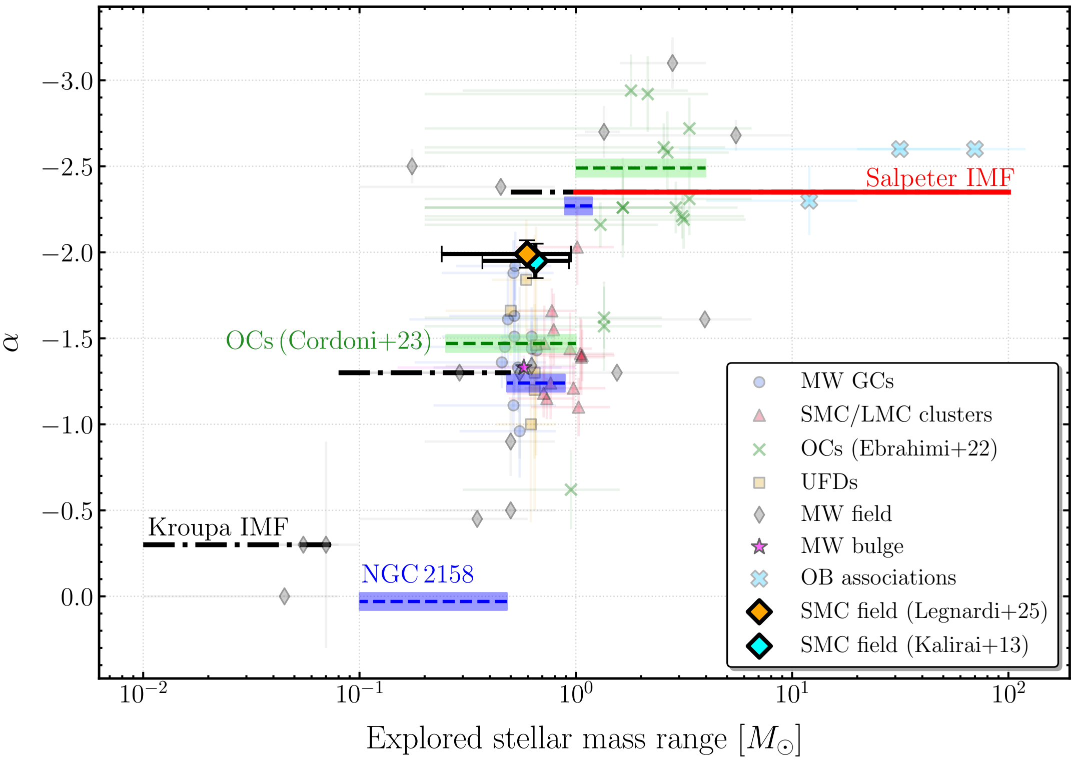

Figure 4.9: The explored stellar mass range of assorted mass functions (adapted from Legnardi et al. [2025]).

regimes: high-mass, low-mass, and very-low-mass. The high-mass and low-mass regime α values are comparable, at ≈-2.27 and ≈-1.24 in this work respectively, and -2.08 ± 0.12 and -1.18 ± 0.04 respectively in Cordoni et al. [2023]. Figure 4.9 shows the explored stellar mass range of NGC 2158 by mass function in comparison with others. The visualization and other data points in Figure 4.9 were provided courtesy of M.V. Legnardi.

5
Conclusion

In this work, I derived high precision photometry and proper motions on deep, multi-epoch images of the intermediate age open cluster NGC 2158. This allowed me to perform a detailed study of binary stars in this cluster as well as the determination of the luminosity and mass functions to $\sim 0.1 M_{\odot}$, a significantly extended mass range.

The color magnitude diagram of NGC 2158 (Figure 4.1) is the most detailed and deepest to date CMD of a massive, intermediate age open cluster. The age of the cluster is approximately 1.9 Gyr, with a metallicity of [Fe/H]$= -0.03$. The main sequence is clear down to $\sim 0.1 M_{\odot}$, which is the first time this has been calculated for an open cluster of this age. Previous studies, even with ACS/WFC data, typically only extend to about $\sim 0.4 M_{\odot}$ (e.g Kalirai et al. [2013]). There is a well separated binary sequence, allowing calculation of the binary fraction for very faint stars. We can also see the white dwarf cooling sequence, some of the stars above the main sequence turn off, and what appear to be some blue straggler stars.

The binary fraction (Figure 4.4) of the full main sequence (17.5 to 24.5 magnitudes, F814W) is 0.19 for mass ratio $q = 0.5$. Above 17.5 magnitudes the binary sequence is less well separated and the main sequence turnoff point interferes in the analysis. When separated into bins of one magnitude, the highest binary fraction is in the range from 17.5 to 18.5: ~ 0.26 for $q = 0.5$. The average stellar mass for that bin is $1.08M_\odot$. The bin with the lowest fraction is from 23.5 to 24.5 magnitudes: ~ 0.12 for $q = 0.5$, with an average stellar mass in the bin of $0.22M_\odot$. The overall trend shows a decrease in the fraction of binaries from higher to lower stellar masses. This reveals a new insight. Compared to other open clusters (Figure 4.5 (a)), NGC 2158 falls within the same relative range in terms of total fraction of binaries. It is notable that this binary fraction trend is consistent with that found in the Galactic field (Figure 4.5 (b)). It is possible that the Milky Way field and open and globular clusters and their differing environments have an effect on binary formation or evolution, but more likely that the limited mass range of previous studies contributes to their findings of a flat trend for binaries over mass range.

The luminosity function (Figure 4.7) and mass function (Figure 4.8) are calculated by separating all stars into bins of one magnitude, from 15.5 to 25.5 magnitudes (Figure 4.6). The number of stars in each bin is carefully corrected for completeness, which was calculated as in Milone et al. [2023] using KS2 and an artificial star analysis. The choice of faintest magnitude for analysis was made based on when the average completeness went below 50%. The average mass of the stars in the brightest bin is $1.07M_\odot$, and in the faintest bin is $0.14M_\odot$. The stellar masses are linearly interpolated from the mass to magnitude relation from the isochrone. The mass function resembles a Kroupa-like mass function. It can be split into three regimes: high-mass, low-mass, and very-low-mass, with slopes found via linear regression to be $\alpha = -2.27$, $\alpha = -1.24$, and $\alpha = -0.03$ respectively. This confirms the result of Cordoni et al. [2023] that the slope of the mass function changes at $\sim 1M_\odot$, and does not show a change in slope at $\sim 0.5M_\odot$ as might be expected from a Kroupa mass function. This work finds an additional change in slope at even lower masses.

This research can be extended to the study of other open and globular clusters, deep multi-epoch data of which already exists in the HST archives. For example, photometry is already available for the open clusters NGC 6819, NGC 6791, NGC 6705, and twelve globular clusters. This would be well suited for a study of binaries at low masses, to further investigate how the binary fraction varies at low stellar masses. Additionally, NIRCam data from JWST will be acquired in late 2025 and early 2026 through programs GO-8960 and GO-9012 (PI Milone), as part of a survey targeting low-mass stars in globular clusters. Another potential analysis includes using Euclid data, which although shallower than HST or JWST data, would enable the detection and characterization of binaries across the full extent of each cluster (see e.g. Milone et al. [2025]). This would allow a study of binaries in relation to radial distance from cluster center.

Data Use Acknowledgments

This research is based on observations made with the NASA/ESA Hubble Space Telescope obtained from the Space Telescope Science Institute, which is operated by the Association of Universities for Research in Astronomy, Inc., under NASA contract NAS 5–26555. These observations are associated with program 10500.

It has also made use of the NASA/IPAC Infrared Science Archive, which is funded by the National Aeronautics and Space Administration and operated by the California Institute of Technology.

This work has made use of data from the European Space Agency (ESA) mission *Gaia* (https://www.cosmos.esa.int/gaia), processed by the *Gaia* Data Processing and Analysis Consortium (DPAC, https://www.cosmos.esa.int/web/gaia/dpac/consortium). Funding for the DPAC has been provided by national institutions, in particular the institutions participating in the *Gaia* Multilateral Agreement.

No generative AI or LLM was used in the writing of this work.

References

Jay Anderson, Ata Sarajedini, Luigi R Bedin, Ivan R King, Giampaolo Piotto, I Neill Reid, Michael Siegel, Steven R Majewski, Nathaniel EQ Paust, Antonio Aparicio, et al. The acs survey of globular clusters. v. generating a comprehensive star catalog for each cluster. *The Astronomical Journal*, 135(6):2055, 2008.

LR Bedin, M Salaris, IR King, Giampaolo Piotto, J Anderson, and S Cassisi. The bottom of the white dwarf cooling sequence in the old open cluster ngc 2158. *The Astrophysical Journal Letters*, 708(1):L32, 2009.

Ralph C Bohlin. Perfecting the photometric calibration of the acs ccd cameras. *The Astronomical Journal*, 152(3):60, 2016.

Giovanni Carraro, Léo Girardi, and Paola Marigo. The intermediate-age open cluster ngc 2158. *Monthly Notices of the Royal Astronomical Society*, 332(3): 705–713, 05 2002. ISSN 0035-8711. doi: 10.1046/j.1365-8711.2002.05326.x.

Giacomo Cordoni, Milone, Antonino P., Marino, Anna F., Vesperini, Enrico, Dondoglio, Emanuele, Legnardi, Maria Vittoria, Mohandasan, Anjana, Carlos, Marilia, Lagioia, Edoardo P., Jang, Sohee, and Ziliotto, Tuila. Photometric binaries, mass functions, and structural parameters of 78 galactic open clusters. *Astronomy & Astrophysics*, 672:A29, 2023. doi: 10.1051/0004-6361/202245457.

Wilton S Dias, Héktor Monteiro, Aandré Moitinho, Jácques RD Lépine, Giovanni Carraro, Ernst Paunzen, Bruno Alessi, and Lázaro Villela. Updated parameters of 1743 open clusters based on gaia dr2. *Monthly Notices of the Royal Astronomical Society*, 504(1):356–371, 2021.

Aaron Dotter, Brian Chaboyer, Darko Jevremović, Veselin Kostov, E Baron, and Jason W Ferguson. The dartmouth stellar evolution database. *The Astrophysical Journal Supplement Series*, 178(1):89, 2008.

Antoine Duquennoy and Michel Mayor. Multiplicity among solar-type stars in the solar neighbourhood. ii-distribution of the orbital elements in an unbiased sample. *Astronomy and Astrophysics (ISSN 0004-6361), vol. 248, no. 2, Aug. 1991, p. 485-524. Research supported by SNSF.*, 248:485–524, 1991.

Anna Frebel and John E. Norris. Near-field cosmology with extremely metal-poor stars. *Annual Review of Astronomy and Astrophysics*, 53(Volume 53, 2015):631–688, 2015. ISSN 1545-4282. doi: https://doi.org/10.1146/annurev-astro-082214-122423.

L Girardi, MAT Groenewegen, E Hatziminaoglou, and L Da Costa. Star counts in the galaxy-simulating from very deep to very shallow photometric surveys with the trilegal code. *Astronomy & Astrophysics*, 436(3):895–915, 2005.

Douglas C Heggie. Binary evolution in stellar dynamics. *Monthly Notices of the Royal Astronomical Society*, 173(3):729–787, 1975.

William Herschel. Xv. account of the changes that have happened, during the last twenty-five years, in the relative situation of double-stars; with an investigation of the cause to which they are owing. *Philosophical Transactions of the Royal Society of London*, 93:339–382, 1803. doi: 10.1098/rstl.1803.0015. URL https://royalsocietypublishing.org/doi/abs/10.1098/rstl.1803.0015.

HST - About. STScI. Date Accessed: 3 Aug 2025. https://www.stsci.edu/hst/about.

Piet Hut, Steve McMillan, Jeremy Goodman, Mario Mateo, ES Phinney, Carlton Pryor, Harvey B Richer, Frank Verbunt, and Martin Weinberg. Binaries in globular clusters. *Publications of the Astronomical Society of the Pacific*, 104 (681):981, 1992.

IRSA. Galactic dust reddening and extinction, 2022.

Heather R Jacobson, Eileen D Friel, and Catherine A Pilachowski. Abundances of red giants in old open clusters. iv. ngc 1817, ngc 1883, ngc 2141, and ngc 2158. *The Astronomical Journal*, 137(6):4753, 2009.

Jason S Kalirai, Jay Anderson, Aaron Dotter, Harvey B Richer, Gregory G Fahlman, Brad MS Hansen, Jarrod Hurley, I Neill Reid, R Michael Rich, and Michael M Shara. Ultra-deep hubble space telescope imaging of the small magellanic cloud: The initial mass function of stars with m 1 m . *The Astrophysical Journal*, 763(2):110, 2013.

Kharchenko, N. V., Piskunov, A. E., Schilbach, E., Röser, S., and Scholz, R.-D. Global survey of star clusters in the milky way - ii. the catalogue of basic parameters . *Astronomy & Astrophysics*, 558:A53, 2013. doi: 10.1051/0004-6361/201322302.

Richard B. Larson. A method for computing the evolution of star clusters. *Monthly Notices of the Royal Astronomical Society*, 147(4):323–337, 04 1970. ISSN 0035-8711. doi: 10.1093/mnras/147.4.323. URL https://doi.org/10.1093/mnras/147.4.323.

M. V. Legnardi, F. Muratore, A. P. Milone, G. Cordoni, T. Ziliotto, E. Dondoglio, A. F. Marino, A. Mastrobuono-Battisti, E. Bortolan, E. P. Lagioia, and M. Tailo. The small magellanic cloud through the lens of the james webb space telescope : binaries and mass function within the galaxy outskirts, 2025. URL https://arxiv.org/abs/2509.08687.

Antonino P Milone, Giacomo Cordoni, AF Marino, F D'Antona, Andrea Bellini, Marcella Di Criscienzo, Emanuele Dondoglio, Edoardo Prospero Lagioia, Norbert Langer, Maria Vittoria Legnardi, et al. Hubble space telescope survey of magellanic cloud star clusters-photometry and astrometry of 113 clusters and early results. *Astronomy & Astrophysics*, 672:A161, 2023.

AP Milone, LR Bedin, Giampaolo Piotto, and Jay Anderson. Multiple stellar populations in magellanic cloud clusters-i. an ordinary feature for intermediate age globulars in the lmc? *Astronomy & Astrophysics*, 497(3):755–771, 2009.

AP Milone, Giampaolo Piotto, LR Bedin, A Aparicio, Jay Anderson, A Sarajedini, AF Marino, Alessia Moretti, Melvyn B Davies, Brian Chaboyer, et al. The acs survey of galactic globular clusters-xii. photometric binaries along the main sequence. *Astronomy & Astrophysics*, 540:A16, 2012.

AP Milone, AF Marino, M Bernizzoni, F Muratore, MV Legnardi, M Barbieri, E Bortolan, A Bouras, J Bruce, G Cordoni, et al. A jwst project on 47 tucanae-binaries among multiple populations. *Astronomy & Astrophysics*, 698:A247, 2025.

Anjana Mohandasan, Antonino P Milone, Giacomo Cordoni, Emanuele Dondoglio, Edoardo P Lagioia, Maria Vittoria Legnardi, Tuila Ziliotto, Sohee Jang, Anna F Marino, and Marília Carlos. Photometric binaries in 14 magellanic cloud star clusters. *Astronomy & Astrophysics*, 681:A42, 2024.

Stella SR Offner, Maxwell Moe, Kaitlin M Kratter, Sarah I Sadavoy, Eric LN Jensen, and John J Tobin. The origin and evolution of multiple star systems. In *Protostars and Planets VII, ASP Conference Series, Vol. 534*, 2023.

Timo Prusti, JHJ De Bruijne, Anthony GA Brown, Antonella Vallenari, C Babusiaux, CAL Bailer-Jones, U Bastian, M Biermann, Dafydd Wyn Evans, L Eyer, et al. The gaia mission. *Astronomy & Astrophysics*, 595:A1, 2016.

Alvio Renzini and Alberto Buzzoni. Global properties of stellar populations and the spectral evolution of galaxies. In Cesare Chiosi and Alvio Renzini, editors, *Spectral Evolution of Galaxies*, pages 195–235, Dordrecht, 1986. Springer Netherlands. ISBN 978-94-009-4598-2.

Devesh P Sariya, Guey Jiang, MD Sizova, ES Postnikova, D Bisht, NV Chupina, SV Vereshchagin, RKS Yadav, G Rangwal, and AV Tutukov. A comprehensive analysis of ngc 2158 in the gaia era: Photometric parameters, apex, and orbit. *The Astronomical Journal*, 161(3):101, 2021.

Michael A Seeds and Dana Backman. *Foundations of Astronomy, Thirteenth Edition.* Cengage Learning, 2016.

Antonio Sollima, Giacomo Beccari, Francesco Rosario Ferraro, F Fusi Pecci, and A Sarajedini. The fraction of binary systems in the core of 13 low-density galactic globular clusters. *Monthly Notices of the Royal Astronomical Society*, 380(2):781–791, 2007.

Stark, D. V., et al., 2024. “ACS Instrument Handbook,” Version 24.0 (Baltimore: STScI).

Antonella Vallenari, Anthony GA Brown, Timo Prusti, Jos HJ De Bruijne, F Arenou, Carine Babusiaux, Michael Biermann, Orlagh L Creevey, Christine Ducourant, Dafydd Wyn Evans, et al. Gaia data release 3-summary of the content and survey properties. *Astronomy & Astrophysics*, 674:A1, 2023.

Acknowledgments

First I would like to thank my advisor, Prof. Antonino Milone, without whom this thesis would not have been possible. That is mainly due to his excellent explanations and advice, but also his willingness to make lots of jokes which is really important for morale. Additionally, everyone in the GALFOR research group for being welcoming and helpful with codes, visualizations, and resources.

Thank you to all my friends and family at home, and to my partner. It turns out that you were right, and that even if it's hard to move across the ocean, I can do it and it's worth it. I did it! But I couldn't have done it without the support from all of you.

Last (but not least) I need to thank a few more people and one item: the friends and classmates I've found during this degree, the Chiucchini/Rangos, the baristas at the coffee shop I go to, and the pistachio-filled croissants they sell there. All in their own ways uniquely indispensable to this experience.